

June 2021

Development of a Bipolar Radiofrequency Ablation Device for Renal Denervation

Noel Perez
University of South Florida

Follow this and additional works at: <https://digitalcommons.usf.edu/etd>

 Part of the [Biomedical Engineering and Bioengineering Commons](#), and the [Electrical and Computer Engineering Commons](#)

Scholar Commons Citation

Perez, Noel, "Development of a Bipolar Radiofrequency Ablation Device for Renal Denervation" (2021).
USF Tampa Graduate Theses and Dissertations.
<https://digitalcommons.usf.edu/etd/9708>

This Dissertation is brought to you for free and open access by the USF Graduate Theses and Dissertations at Digital Commons @ University of South Florida. It has been accepted for inclusion in USF Tampa Graduate Theses and Dissertations by an authorized administrator of Digital Commons @ University of South Florida. For more information, please contact scholarcommons@usf.edu.

Development of a Bipolar Radiofrequency Ablation Device for Renal Denervation

by

Noel Perez

A dissertation submitted in partial fulfillment
of the requirements for the degree of
Doctor of Philosophy
Department of Electrical Engineering
College of Engineering
University of South Florida

Major Professor: Stephen E. Sadow, Ph.D.
Karl Muffly, Ph.D.
Gokhan Mumcu, Ph.D.
Mark Jaroszeski, Ph.D.
Andrew Hoff, Ph.D.

Date of Approval:
June 30, 2021

Keywords: Basket catheter, high blood pressure, hypertension, resistant hypertension

Copyright © 2021, Noel Perez

Dedication

I dedicate my dissertation work to my wife, whose motivation and unconditional support were key to keep me motivated and perseverant.

Acknowledgments

I wish to thank my committee members, who were more than generous with their expertise and valuable time. A special thanks to Dr. Stephen Sadow, my advisor, for his continuous support, motivation, problem-solving, and most of all, his unconditional support throughout the entire process.

Table of Contents

List of Tables	iii
List of Figures	iv
Abstract	vii
Chapter 1: Introduction	1
1.1 Clinical Relevance of Hypertension.....	1
1.2 The Sympathetic Nerve System and Hypertension.....	2
1.3 History of Renal Denervation	5
1.4 The Resurgence of Renal Denervation for the Treatment of Hypertension	6
1.5 Renal Denervation Clinical Trials in the USA	9
1.6 Motivation	11
1.7 Summary and Dissertation Organization.....	11
Chapter 2: Design of a Radiofrequency Ablation Device via Numerical Simulation and Finite Element Modeling	13
2.1 Computational Model Introduction	13
2.2 Modeling the Renal Artery, Surrounding Tissue, and Bipolar Electrodes	14
2.2.1 Build the Geometry	14
2.2.2 Electrical and Thermal Properties of Components	18
2.2.3 Electric Field	19
2.2.4 Bioheat Equation	23
2.2.5 Boundary Conditions	24
2.2.6 Ablated Tissue Definition	25
2.2.7 Computational Model Summary	25
2.3 Numerical Simulation Results.....	26
2.4 RF Ablation Catheter Design and Build	30
2.5 Summary.....	32
Chapter 3: <i>In Vitro</i> Tissue Phantom Experiments	34
3.1 Thermochromic Phantom (TCP) Tissue	34
3.2 TCP Tissue Formulation and Preparation	35
3.3 Radiofrequency Ablation of TCP Tissue	36
3.4 Determination of TCP Tissue Ablation Zone.....	38
3.5 Comparison Between <i>In Silico</i> and <i>In Vitro</i> Results.....	39
3.6 Summary.....	42

Chapter 4: <i>Ex Vivo</i> Porcine Tissue Experiments	43
4.1 Porcine Renal Artery Preparation.....	43
4.2 Radiofrequency Ablation of Porcine Renal Artery Tissue.....	45
4.2.1 First <i>ex vivo</i> RF Ablation Experiment	45
4.2.2 <i>Ex vivo</i> Ablated Tissue Storage and Handling	46
4.2.3 First Histology Results.....	46
4.2.4 Investigation of Porcine Tissue Electrical Characteristics	47
4.2.5 Updated FEM Model	53
4.2.6 Second <i>ex vivo</i> RF Ablation Experiment.....	54
4.2.7 Second Histology Results	54
4.3 Comparison Between <i>In Silico</i> , <i>In Vitro</i> and <i>Ex Vivo</i> Results.....	56
4.4 Summary.....	57
 Chapter 5: Conclusion and Future Work.....	 58
5.1 Summary.....	58
5.1.1 <i>In Silico</i> , <i>In Vitro</i> and <i>Ex Vivo</i> RF Ablation Analysis and Comparisons	58
5.2 Discussion.....	59
5.3 Conclusion	62
5.4 Future Work	62
 References.....	 64
 Appendix A: Copyright Permissions.....	 71
 About the Author.....	 End Page

List of Tables

Table 1.1	Comparison of CE-marked renal denervation catheters.	9
Table 2.1	Electrical and thermal properties of components at 500 kHz.	18
Table 2.2	Skin depth and complex conductivity of components at 500 kHz.	21
Table 2.3	Thermal tissue damage threshold parameters.....	25
Table 3.1	Thermochromic phantom tissue recipe.....	34
Table 3.2	Comparison of ablated zone dimensions between <i>in silico</i> and <i>in vitro</i> models.	39
Table 4.1	Complex Permittivity of TCP and porcine tissue at 200 MHz.....	49
Table 4.2	Electrical Parameters of TCP and porcine tissue at 200 MHz.	50
Table 4.3	RF Ablation Power Comparison.....	53
Table 4.4	Comparison of ablation zone ^a between <i>in silico</i> , <i>in vitro</i> , and <i>ex vivo</i> experiments.	56

List of Figures

Figure 1.1	Diagram representation of the divisions in the human nervous system.....	3
Figure 1.2	Pictorial representation of afferent and efferent innervation surrounding the renal artery.....	4
Figure 1.3	Physiological diagram of the renal artery and circumferential peri-arterial nerve location.	5
Figure 1.4	Pictorial representation of an RF ablation device is inserted through the femoral artery for a renal ablation of the sympathetic nerve.	7
Figure 1.5	RD procedure using a guided sheath to maneuver the RF ablation catheter inside the renal artery (A).....	8
Figure 2.1	Cylindrical representation of the blood inside the renal artery with an average diameter of 4.1 mm and length of 31 cm.	14
Figure 2.2	Cylindrical representation of the renal artery wall with a thickness of 0.5 mm enclosing the renal blood volume from Fig. 2.1.....	15
Figure 2.3	Cylindrical representation of the connective tissue surrounding the renal artery model of Fig. 2.2.....	16
Figure 2.4	Innovative bipolar electrode design (patent pending) [36] focuses current density towards the artery wall and surrounding tissue in the renal artery.....	17
Figure 2.5	Final geometric model of the renal artery with blood, surrounding tissue, and bipolar electrodes in contact with the artery wall.....	17
Figure 2.6	Numerical solution of model with 60 Vp-p and current density with bipolar electrodes.....	27
Figure 2.7	Numerical solution of model showing in the isothermal surface graphic the ablated surrounding tissue heated to more than 60°C and less than 90°C.....	28
Figure 2.8	Isothermal surfaces filtered for the effective ablation temperature of 60°C and 90°C.....	28

Figure 2.9	Height and length dimensional measurements of the ablation zone from the numerical model after 60 seconds of ablation.	29
Figure 2.10	Width dimensional measurements of the ablation zone from the numerical model after 60 seconds of ablation.	29
Figure 2.11	Graphical representation of the basket catheter with three splines and two electrodes per spline.....	30
Figure 3.1	Color chart of TCP tissue for temperatures between 25°C and 75°C.....	34
Figure 3.2	<i>In vitro</i> setup for the ablation of Thermochromic phantom (TCP) tissue.....	36
Figure 3.3	Simplified diagram of the <i>in vitro</i> setup for the ablation of the thermochromic phantom (TCP) tissue.	36
Figure 3.4	Bipolar ablation zone of TCP tissue with the temperature reaching $\geq 60^{\circ}\text{C}$ is approximately (A) 2 mm (W) x (B) 9 mm (L) x (C) 2 mm (H).	37
Figure 3.5	Side by side comparison of <i>in silico</i> isothermal surfaces and <i>in vitro</i> TCP tissue thermal changes.	38
Figure 3.6	FEM model prediction of blood temperature after 60 seconds of RF ablation inside renal artery flowing from the negative to positive electrode	40
Figure 4.1	<i>Ex vivo</i> experimental tissue samples of porcine kidneys.	43
Figure 4.2	<i>Ex vivo</i> experimental tissue samples of porcine renal arteries.	43
Figure 4.3	<i>Ex vivo</i> experiment setup for the ablation porcine renal artery tissue.	44
Figure 4.4	Photograph of RF ablated <i>ex vivo</i> renal nerve tissue section of Fig. 4.3(b) stored in a 10% neutral buffered formalin solution for histology evaluation.	45
Figure 4.5	Two (2) optical micrographs of RF ablated <i>ex vivo</i> renal nerve sections after tissue histology.	46
Figure 4.6	Permittivity measurements of (A) TCP phantom and (B) <i>ex vivo</i> porcine tissue.....	47
Figure 4.7	Real part (ϵ') of the measured tissue permittivity of fresh porcine tissue (red), preserved porcine tissue (green), and TCP tissue (blue) as a function of frequency (Hz).....	48

Figure 4.8	Imaginary part (ϵ'') of the measured tissue permittivity of fresh porcine tissue (red), preserved porcine tissue (green), and TCP tissue (blue) as a function of frequency (Hz).....	48
Figure 4.9	Frequency response of the RF linear amplifier Pendulum F20A (Pendulum, Stockholm, Sweden) as a function of load and input voltage.	51
Figure 4.10	RF ablation voltage and current as a function of time.	52
Figure 4.11	H&E histological sections were strategically dissected over the ablated zone	54
Figure 4.12	Second <i>ex vivo</i> tissue ablation H&E-stained sections taken from over the positive electrode.	55
Figure 4.12	Control histology H&E-stained sections of the second <i>ex vivo</i> tissue ablation took from an inactive positive electrode.....	55

Abstract

The American Heart Association (AHA) reported in March 2020, hypertension (HT) is a major risk factor for cardiovascular diseases and heart stroke. Resistant hypertension (RH) is a subset of HT and affects 11-16% of hypertensive patients. RH is diagnosed when a patient cannot achieve blood pressure control despite taking three or more medications and is a serious clinical management challenge.

Renal denervation (RD) using radiofrequency (RF) ablation is an accepted form of RH therapy. RD devices are typically delivered through femoral access into the renal artery with the assistance of a standard guided sheath. In the European Union (EU), the approved RD devices are mostly single electrodes with a ground pad over the exterior body with the risk of skin burns. Other RD devices incorporate an inflatable balloon that risks blocking renal blood flow during treatment.

At the time of this dissertation research, the Food and Drug Administration (FDA) has not approved any RD device for use in the USA except for investigational purposes. Human trials started with the well-known Symplicity HTN-1 (Medtronic, Dublin, Ireland) treating enrolled patients in June 2007, and results were promising. Trials continued with HTN-2 then HTN-3 (Funded by Medtronic; SYMPPLICITY HTN-3 ClinicalTrials.gov, NCT01418261), which did not significantly reduce HT in a sham control study. All the human trials were performed with unipolar with grounding pad RD devices. Therefore, new devices that focus energy on the ablation zone without the risks of skin burn from grounding pads and without compromising renal blood flow are urgently required.

A basket catheter with bipolar electrodes has been developed to perform targeted controlled ablation through Joule heating induction resulting in tissue temperature increased within the range of 60°C to 100°C starting from the normal body temperature of 37°C as a baseline. In this research, the following contributions to the state of the art have been made: (1) novel electrode design whereby the dimensions and geometry were successfully simulated and optimized via finite element model (FEM) based computer simulation, (2) simulations included both the surrounding artery and connective tissue electrical properties to predict the ablation zone dimensions to achieve renal nerve ablation, (3) a Thermo-Chromic Phantom (TCP) tissue phantom was used to validate the in-vitro ablation zone with the computer FEM model, (4) the geometry, shape, and form of the ablation zone were visually compared to simulations and demonstrated high concordance indicating that the computer model was valid, (5) electrode design over basket catheter splines does not require a balloon, so it has the advantage of no renal artery blood flow blockage during ablation, and bipolar electrode design does not require a grounding pad resulting in the elimination of skin burns risks. Furthermore, there is no need for active cooling, and the catheter has short ablation times and the lowest power requirement of existing designs to perform the ablation.

The bipolar RF ablation electrode deserves further research and development as a potential alternative to catheter-based RD *in vivo* devices. The bipolar configuration and innovative design presented in this study ensure that the current density is focused on the target tissue, thus reducing the energy transferred to renal blood. Furthermore, the computational RF ablation model estimates renal artery ablation zones for highly targeted renal denervation in patients with resistant hypertension.

Chapter 1: Introduction

1.1 Clinical Relevance of Hypertension

Hypertension (HT), more commonly referred to as high blood pressure (HBP), is a long-term medical condition in which blood pressure (BP) inside the arteries increases at systolic blood pressure (SBP) values of more than or equal to 140 mm Hg and/or diastolic blood pressure (DBP) values of more than or equal to 90 mm Hg. HT prevalence worldwide was estimated at 1.13 billion people in 2015 and predicted to increase by 15 to 20% by 2025, reaching close to 1.5 billion adults. Hypertension becomes progressively more common with advancing age, with a prevalence of more than 60% in adults aged over 60 years [1].

In the USA, it is estimated that 32% of the adult population, or one in every three (3) adults, suffers from HT. Unfortunately, less than half of the hypertensive adults have the condition under control, which has caused a financial burden of approximately \$48.6 billion per year. In addition, HT was the primary, or contributing, cause of death for 410,000 Americans in 2014, or more than 1,100 deaths per day [2].

The American Heart Association (AHA) / American College of Cardiology guidelines diagnose resistant hypertension (RH) when an adult needs three or more medications to treat HT but still has a BP that exceeds the goal of 130 mm Hg SBP or 80 mm Hg DBP. According to the scientific statement published in the Associations' journal Hypertension, RH affects 12-15% of patients treated for HT. The AHA estimates that 50-80% of patients who should be taking BP-lowering drugs do not follow the regimen [3]. Patients lack adherence to a HBP pharmaceutical

regimen because of the enormous pill burden, the complexity of doses, out-of-pocket medical costs, adverse reaction to other medications, among other factors [4].

1.2 The Sympathetic Nerve System and Hypertension

The human nervous system is the control center of the body and comprises two main parts: the central nervous system (CNS) and the peripheral nervous system (PNS). The CNS is the nervous system's processing center, and PNS connects the CNS to the body's limbs and organs. The CNS is divided into the brain and the spinal cord. The brain is the center of the nervous system and is where most processing occurs, such as thought, emotion, and body's activity coordination. The spinal cord serves as the connection between the brain and the body for bidirectional signal connectivity. The PNS is divided into the somatic nervous system (SNS) and the autonomic nervous system (ANS). The SNS controls voluntary activities such as musculoskeletal movements, and the ANS controls involuntary activities such as respiration, digestion, or blood pressure.

Finally, the ANS is divided into the parasympathetic and sympathetic nervous systems. The parasympathetic system is involved during rest and digest activities. The sympathetic system is the opposite of the body at rest, and it reacts under stress by increasing respiration rate, heart rate, or blood pressure. Therefore, it is the "fight-or-flight" response of the sympathetic nervous system [5].

Figure 1.1 illustrates the major components and functions of the CNS. The autonomic sympathetic nervous system of the PNS is the center of interest for this research since it correlates to blood pressure regulation through an involuntary action of body signals. In addition, understanding the mechanism of the signals interacting with the CNS to control blood pressure can help identify alternatives to pharmaceutical treatment via manipulation of this CNS function.

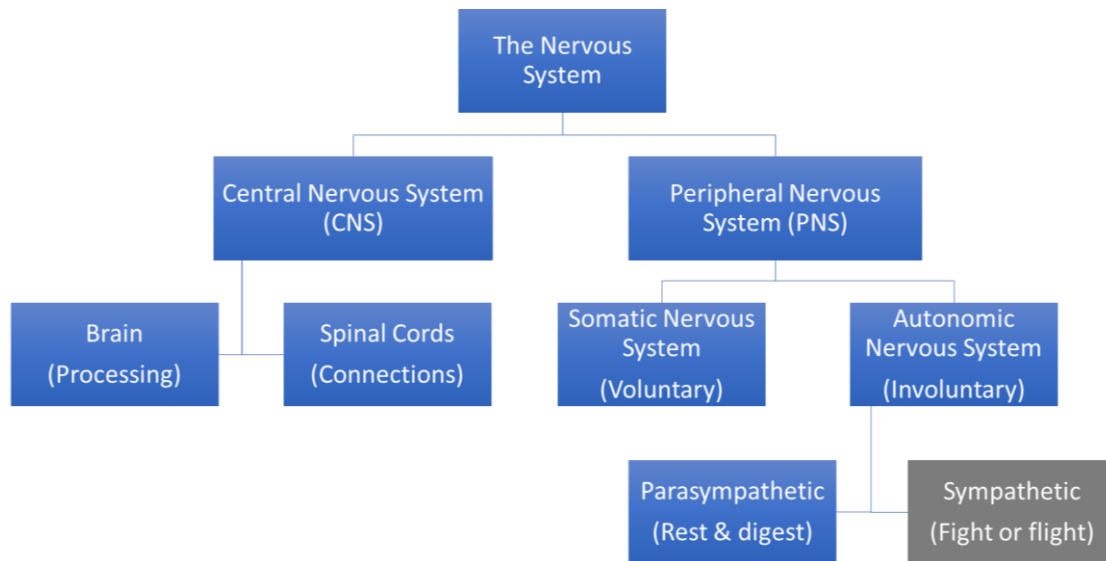


Figure 1.1 Diagram representation of the divisions in the human nervous system. The sympathetic system performs involuntary control of systems such as blood pressure.

The renal arteries are innervated with afferent and efferent nerves as part of the sympathetic nervous system, as depicted in Figure 1.2, enabling a bidirectional communication link between the brain and the kidneys [6]. The nerves around the renal arteries transmit the “fight-or-flight” signaling of the autonomic nervous system [7]. The afferent and efferent nerves signals are the input/output, respectively, to/from the brain for autonomic information processing. The signals operate as a negative feedback automatic control system. When the input (afferent) signal lowers, the ANS reacts by increasing the output (efferent) until the ANS returns to equilibrium (or zero error) between the input and output sympathetic signals. High efferent signals release vasoconstrictor enzymes, increase sodium/water retention, and increase heart pumping force to increase blood pressure [8]. Therefore, a high efferent signal causes the afferent signals to lower, restoring blood pressure to baseline. The automatic control is attenuated with [9]:

- Renal ischemia – blood deficiency
- Hypoxia – oxygen deprivation
- Oxidative stress – an imbalance of free radicals [10]

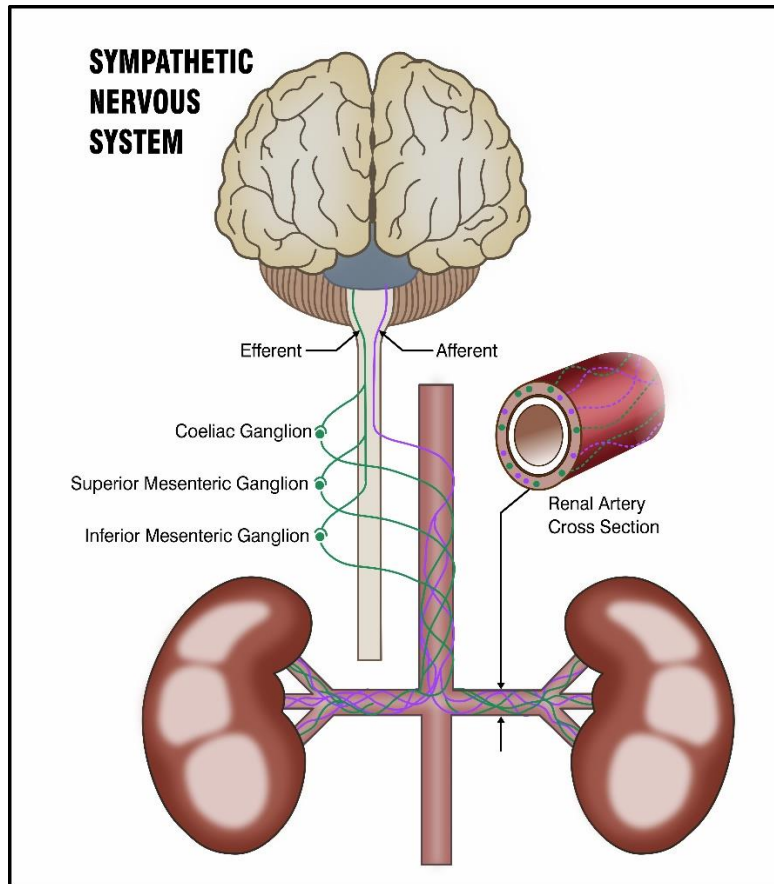


Figure 1.2 Pictorial representation of afferent and efferent innervation surrounding the renal artery. Note. From [6]. © Elsevier. Used with permission.

The anatomic distribution of the afferent and efferent nerves surrounding human renal arteries has been characterized in a study that collected 40 renal arteries from 20 autopsy subjects [11]. The study identified the area with the highest renal sympathetic nerves within a distance of 1 to 4 mm from the abdominal aorta (proximal) and between 3.1 to 3.4 mm from the renal artery, as illustrated in Figure 1.3. The study also identified that renal nerves were dominantly composed of efferent rather than afferent nerves. The efferent nerves drive the kidneys' signals for either increasing or reducing BP as a mechanism for the "fight-or-flight" ANS.

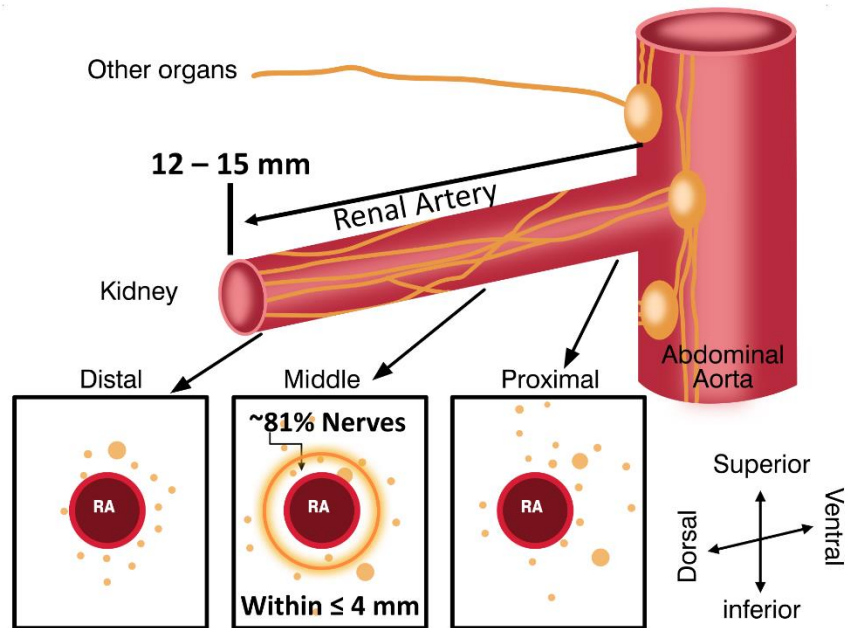


Figure 1.3 Physiological diagram of the renal artery and circumferential peri-arterial nerve location. Note. From [11]. © Elsevier. Used with permission.

1.3 History of Renal Denervation

In 1889, experiments with dogs reported that stimulation of renal nerves caused changes in canine BP [12]. In the following decades, additional studies were reported on animals, but it was not until 1923 that researchers independently suggested neurosurgical treatment of HT in humans [13]. In 1925 Adson was the first to perform a surgical sympathectomy (disconnection of the sympathetic nerve at the trunk) to treat HT [14]. During the following years and into the 1930s, multiple sympathectomy surgeries were reported for treating HT [15]. A variation of sympathectomy (renal decapsulation) reported a significant but short-term reduction in BP, which targeted the nerves between the capsule and the renal cortex [16]. The first case of bilateral renal denervation (RD) to treat HT was reported in 1934 and established that the procedure was safe and had no adverse effect on renal function [17]. In 1935, five patients underwent bilateral RD, and a decrease in BP that lasted for months in the majority of those patients was reported [18].

Surgical RD and its impact on BP foster procedures to move into a more radical sympathectomy procedure – the surgical removal of splanchnic nerves (i.e., a splanchnicectomy), which showed dramatic results in most patients with HT [19]. For the subsequent two decades, surgical sympathectomy (thoracolumbar splanchnicectomy) became the preferred procedure to treat HT patients not responding to diet or then-limited pharmacological therapy [20].

Between 1938 and 1947, approximately 2,400 patients with HT underwent surgical sympathectomy lumbar splanchnicectomy [21]. Although a significant BP reduction was reported, an important complication, postural hypotension, was identified after the surgery [22]. In the mid-1950s, the first HT drug, Diuril® [23], became available, and, for the first time, a drug regimen therapy replaced surgical splanchnicectomy for the next five decades [24].

1.4 The Resurgence of Renal Denervation for the Treatment of Hypertension

In 1987, published results from a thesis demonstrated that electric stimulation of afferent sympathetic nerves could reduce BP in a dose-dependent manner [25]. The results also demonstrated that BP responses could be disconnected by spinal interruption of the efferent sympathetic nerves, which travel through the spine. In addition, afferent renal nerves resection through ventral rhizotomy prevented the development of HT in rats with chronic renal insufficiency [26]. In other studies, patients who had undergone bilateral nephrectomy, in which removal of kidneys will interrupt both the afferent and efferent renal sympathetic nerves, displayed significantly lower BP [27].

A resurgence on renal denervation for hypertension treatment was reinforced with the initial evidence of the benefits from RD during kidney transplants with end-stage renal failure, which improved blood pressure control [28]. The RD procedure disconnects or “open circuits” both efferent and afferent sympathetic nerves to the kidneys, therefore disconnecting the signals

that trigger increased blood pressure. RD has been performed, through the years, both in experimental models and in humans by surgical exposure of renal nerves [20]. The renal nerves were interrupted mainly using a surgical scalpel resulting in lengthy and high-risk procedures.

Advances in catheter-based technologies made feasible minimally invasive access to internal organs through the vascular system. Destino™ Reach (Oscor, Inc., Palm Harbor, Florida) is an 8.5F bi-directional steerable guiding sheath that can reach the renal artery to deliver a RD catheter through the femoral access, as shown in Figure 1.4. Therefore, it is presently a commercialized alternative to access the renal nerves from the “inside” of the renal artery and perform the RD with an energy source replacing the invasive scalpel method. As a point of reference, catheter-based radiofrequency (RF) ablation techniques have been used in Electrophysiology for more than two decades in cardiovascular applications such as ventricular arrhythmia [20].

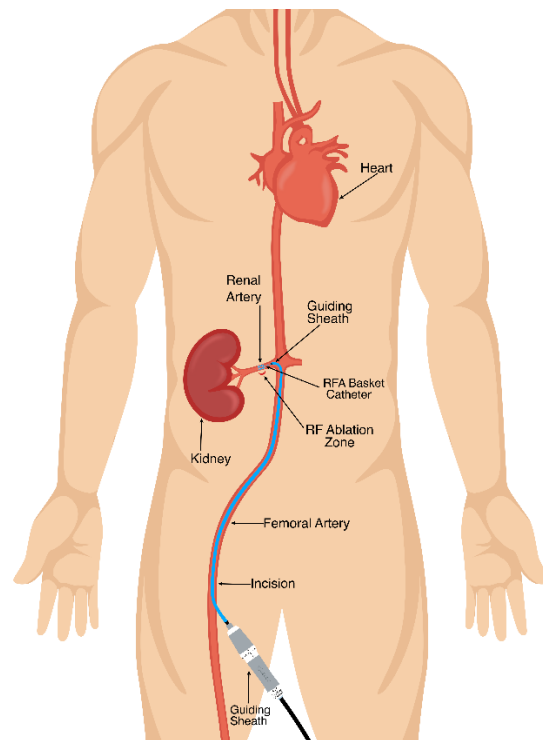


Figure 1.4 Pictorial representation of an RF ablation device is inserted through the femoral artery for a renal ablation of the sympathetic nerve.

Recent investigations have been published using different energy sources to perform RD, such as radiofrequency (RF), ultra-sound, cryogenics, and chemical [30]. An important observation common from all ablations is that the lesions cannot be performed at the same cross-section of the vessel, as shown in figure 1.5. A complete 360 degrees circumferential ablation has been found to increase the risk of renal artery stenosis – a narrowing of the artery – which defeats the purpose of RD and could result in an increase of high blood pressure. The discrete lesion goal is to “open circuit” the efferent and afferent renal nerves between the kidneys and the sympathetic system to reduce BP without renal artery stenosis [20].

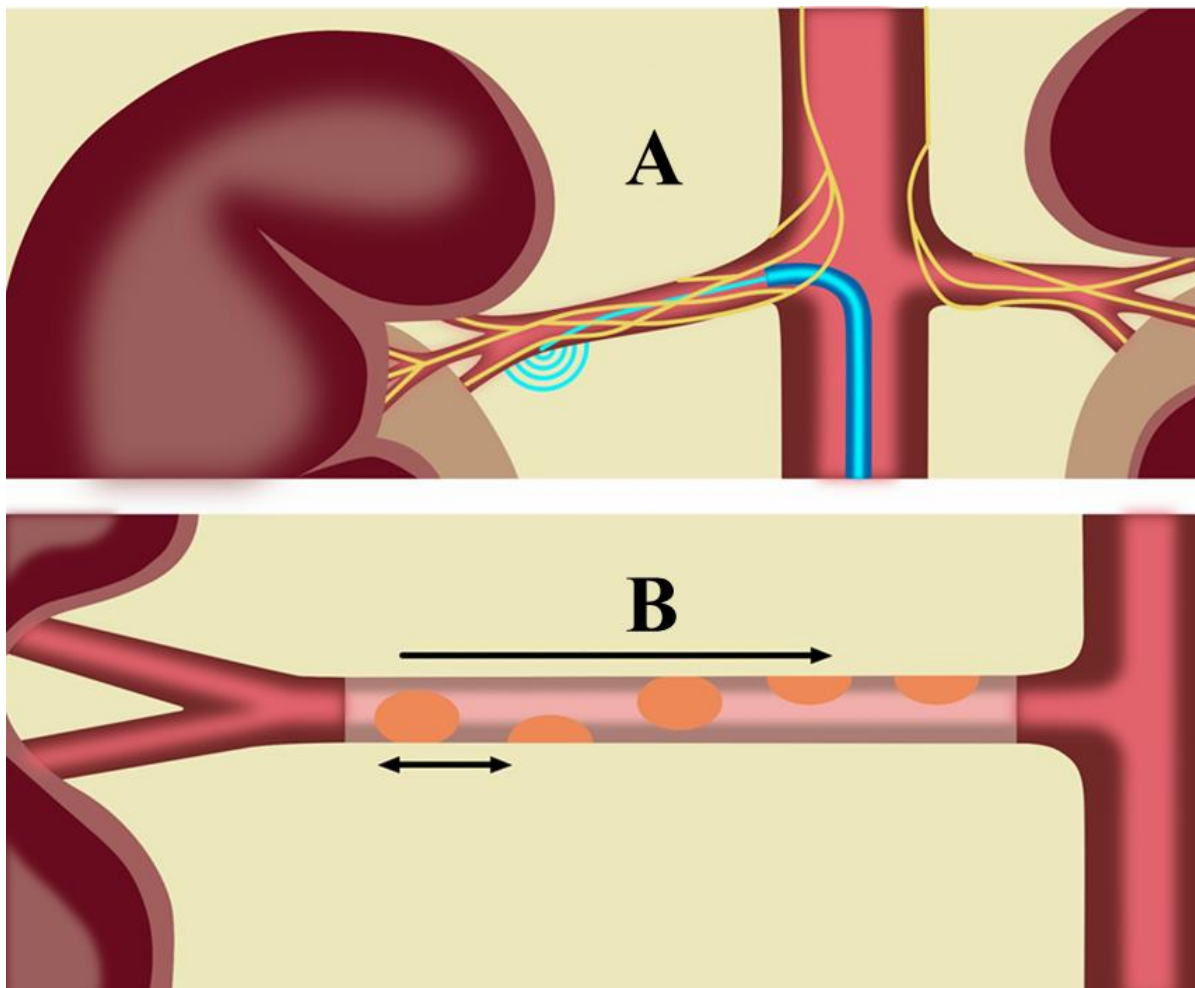


Figure 1.5 RD procedure using a guided sheath to maneuver the RF ablation catheter inside the renal artery (A). The circles in (B) indicate a displaced pattern of RF ablations along the renal artery. Note. From [31]. © Dove Medical Press. Used with permission.

1.5 Renal Denervation Clinical Trials in the USA

As of December 2015, six (6) medical device companies received the Conformité Européenne approval (CE mark) to perform RD in the European Union, each with unique design variations. Table 1 lists the device's brand names from each company that has been awarded the CE mark: the Symplicity™ and the Spyral™ (Medtronic, Dublin, Ireland), the Vessix™ (Boston Scientific, Marlborough, MA, USA), the EnligHTN™ (St. Jude Medical, St. Paul, Minnesota), the Iberis™ (Terumo Medical Corporation, Tokyo, Japan), and the Paradise™ (Recor, Amsterdam, the Netherlands). The Food and Drug Administration (FDA) has cleared no RD device for use in the USA except for investigational purposes [32].

Table 1.1 Comparison of CE-marked renal denervation catheters. Note. From [32]. © Dove Medical Press. Used with permission.

Catheter	Energy	Configuration	Electrode	Balloon	Cooling	Delivery	Ablation time (s/artery)	Max. power (W)	Vascular access (Fr)
Symplicity™ (Medtronic)	RF	Unipolar	Single	No	Blood	Deflectable tip	540	8	6
Spyral™ (Medtronic)	RF	Unipolar	Multiple	No	Blood	Monorail	60	8	6
Vessix™ (Boston Scientific)	RF	Bipolar	Multiple	Yes	None	Over-the-wire	30	1	8
EnligHTN™ (St Jude)	RF	Unipolar	Multiple	No	Blood	Delectable tip	90	6	8
Iberis™ (Terumo)	RF	Unipolar	Single	No	Blood	Delectable tip	540	8	4
Paradise™ (Recor)	US	Unipolar	Single	Yes	Close irrigated	Over-the-wire	50-150	30	6
This research	RF	Bipolar	Multiple (2 to 16)	No	Not required	Guided sheet	60	<1	6

The first human trial results for renal denervation in the USA started with the well-known Symplicity™ HTN-1 and revived the medical device industry's interest in the minimally invasive

treatment of HT. While performed on a relatively small patient group, the HTN-1 study suggested that RD using a single electrode catheter appeared safe and significantly reduced in-office blood pressure at 6-, 12-, and 36-months post-intervention, respectively was reported [28].

The subsequent Symplicity™ HTN-2 was designed as a randomized, controlled clinical trial that compared a renal denervation group with a conventional treatment group. However, the HTN-2 trial raised some concerns based on the observed discrepancy between ambulatory and office blood pressure reduction after renal denervation, which was more significant than other unblinded drug trials [28]. Therefore, the observed BP reduction in the renal denervation group might have been influenced by the so-called Whitecoat effect [20].

Symplicity™ HTN-3 — the most extensive and first study to include a sham control — was performed as a third phase trial but failed to demonstrate a blood pressure-lowering effect beyond that observed in the sham control group. Simplicity™ HTN-3 showed that RD was not superior to drug therapy and provided possible reasons for this conclusion such as incomplete denervation, operator inexperience, improper selection of patients, and faulty design of the study itself. However, HTN-3 failure led to improved and redesigned the ablation catheter from a single point ablation electrode to 4-quadrant bilateral renal nerve ablation of the principal plus accessory renal arteries [28].

The fourth human trial, named Spyral™ HTN-OFF MED, yielded single-digit blood pressure reduction instead of the observed double-digit reduction in the HTN-1, HTN-2, and HTN-3 studies [28]. In all previous trials, the RD device was a unipolar electrode with an external grounding pad with variations of single to multiple electrodes.

Clearly, there is hope that the suitable RD device can be designed and used to lower patient blood pressure as a minimally invasive therapy to treat HT.

1.6 Motivation

Resistant hypertension (RT) is currently a prevalent condition with unmet clinical solutions that requires further attention. Current treatments with pharmaceuticals are not addressing most of the population with this potentially fatal condition either due to ineffectiveness of drugs or behavioral burden. An alternative to drug regimen therapy could benefit high blood pressure patients, including the higher risk population with resistant hypertension.

The latest advances in minimally invasive endovascular catheter-based devices have increased research interest in renal sympathetic nerves interaction with the development and maintenance of HPB [24]. Therefore, RD has re-emerged as a viable alternative, especially for high-risk patients with RH [45]. This research aims to develop an effective catheter-based RD device to reduce blood pressure using a more accurate basket catheter design with multiple electrodes to allow for custom-RD of a patient's renal artery nerves without any deleterious effects on the artery wall and surrounding tissue. This design will aim to develop a bipolar electrode design capable of ablating the tissue. Then multiple bipolar electrodes will be assembled over multiple splines distributed circumferentially and longitudinal on each spline to provide a complete 360 degrees coverage of the renal artery. Finally, the electrodes are terminated with an electrical connector to a future-developed switching system to change from mapping to ablation and vice versa. This design could provide further research for mapping bio-signals of the sympathetic activity to determine the appropriate location for targeted ablation.

1.7 Summary and Dissertation Organization

This work resulted in a radiofrequency (RF) ablation catheter design (patent pending) [36] that can be delivered through femoral access into the aorta artery and perform RD from inside the

renal artery for the treatment of hypertension. In addition, the design incorporates enhanced features over existing RD devices such as:

- Low power requirements (≤ 1.0 W)
- Does not entirely block the renal flow during the procedure
- Directs the Joule heating to the denervation area only
- Incorporate multiple bipolar electrodes circumferentially
- Does not require an external body grounding pad

Table 1.1 compares this design's main characteristics to the devices currently approved in the EU (CE mark) but not approved in the USA except for experimental purposes.

This dissertation is organized as follows: Chapter 1 introduces renal denervation as a means to treat hypertension and elaborates on the RF ablation catheters commercially available in Europe. Finite element modeling of renal artery RF ablation is presented in Chapter 2. In Chapter 3, the computer model is validated with an *in vitro* tissue phantom that incorporates a thermochromic additive to allow for quick visual observation of the ablation zone. After the computer model is refined through multiple iterations with the phantom tissue, the model is compared with *ex vivo* tissue ablations in Chapter 4 for further confirmation. Finally, chapter 5 summarizes the ablations performed *in silico*, *in vitro*, and *ex vivo* of the new RF ablation catheter design (patent pending) [36], provides a discussion and summary of the research performed, and an elaboration of the future works that need to be performed to bring this technique to the biomedical device market.

Further studies are warranted to test the RF ablation basket catheter *in vivo* with porcine animals. In addition, the electrodes can be further studied for the capability of sensing sympathetic bio-signals in an effort to map the activity and compare before-after RF ablation for a means to determine effective renal sympathetic nerve ablation.

Chapter 2: Design of a Radiofrequency Ablation Device via Numerical Simulation and Finite Element Modeling

2.1 Computational Model Introduction

Advanced numerical simulations provide the best means to optimize the design of an RF ablation catheter. Computerized finite element modeling (FEM) provides a versatile, agile, and cost-effective platform to perform multiple design iterations and better understand the expected results before moving into prototype build. In addition, the FEM environment allows design optimization at a much lower cost than the trial-and-error method with physical prototypes allowing quick modifications and updates to the results.

The modeling workflow of COMSOL Multiphysics® software [33] was followed to build the geometric objects, specify material properties, define physical boundary conditions, create a numerical model, spatial mesh, and obtain solutions. The geometry was in three dimensions (3D) and included the bipolar electrodes, renal artery with blood flow, and surrounding connective tissue. Three Multiphysics® modules were utilized in the simulation: Electric Currents, Bioheat Transfer, and Heat Transfer. The electric currents module solves the induced electric fields in the frequency domain while the heat transfer module performs a transient analysis of the ablation resulting from the electric fields.

The model simulation provided a faster environment to optimize the bipolar electrode design and predict ablation zone volume within the connective tissue. Once the model is validated with *ex vivo* and *in vivo* testing, the model will help investigate other tissues and electrode designs.

2.2 Modeling the Renal Artery, Surrounding Tissue, and Bipolar Electrodes

The renal artery and surrounding connective tissue were modelled with cylindrical geometry approximations. The geometry was built starting from the inner components and continued until the outermost component. The last step was to add the bipolar electrode into the renal artery. The blood inside the artery was first defined, followed by the renal artery wall and the surrounding connective tissue.

2.2.1 Build the Geometry

A cylinder was used to represent the renal blood, as shown in Figure 2.1, with a diameter of 4.1 mm, representing the average diameter of the renal artery for adults at the distal segment from the aorta [34]. The length of the cylinder is 20 mm representing a section of 31 cm average length of renal artery for adults [34].

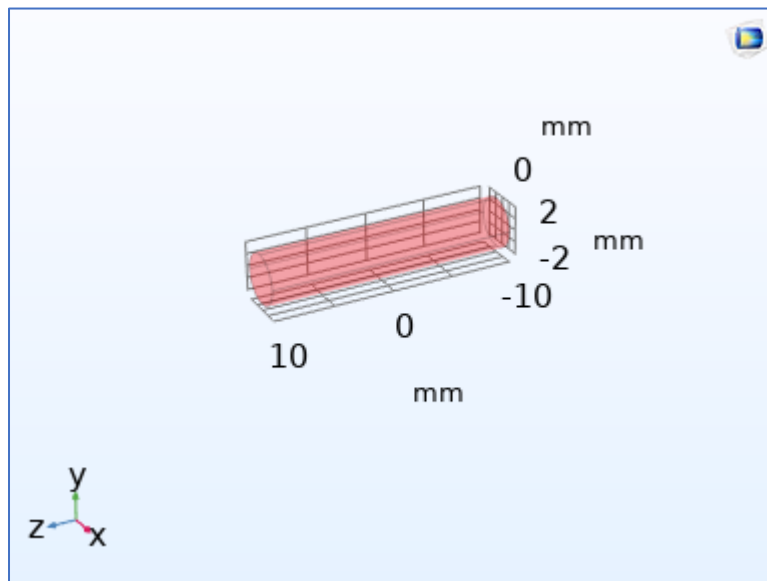


Figure 2.1 Cylindrical representation of the blood inside the renal artery with an average diameter of 4.1 mm and length of 20 mm. Image from COMSOL Multiphysics® software.

Next, another cylinder, shown in Figure 2.2, is drawn surrounding the blood to represent the renal artery wall composed of tunica intima and media with a maximum thickness of 0.5 mm [35].

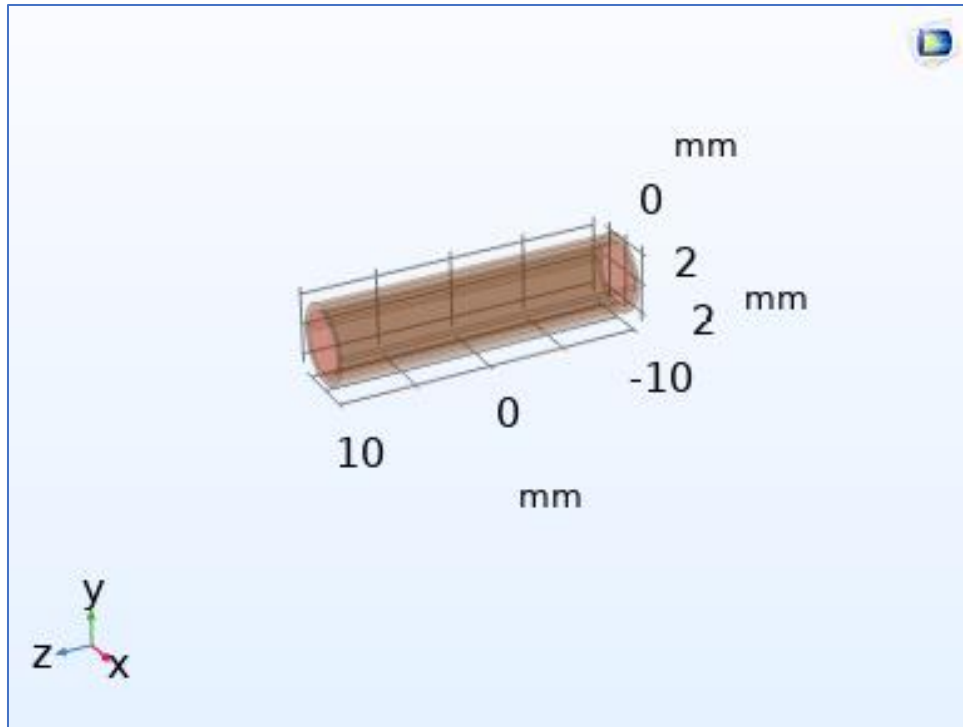


Figure 2.2 Cylindrical representation of the renal artery wall with a thickness of 0.5 mm enclosing the renal blood volume from Fig. 2.1. Image from COMSOL Multiphysics® software.

The next step is to model the connective tissue surrounding the renal artery wall, as shown in Figure 2.3. The final model dimensions are 20 mm x 20 mm x 20 mm and include an infinite element domain (IED) at the model's geometrical borders. The IED is an artificial boundary used to delimit the zone of interest to a small section of the renal artery and limit the extent of the renal system simulated to the target ablation zone. This results in more efficient utilization of computing resources during simulation by eliminating the need to define larger dimensions of surrounding tissues and prevent edge effects from influencing the zone of interest.

The model provides the advantage of adjusting the geometry and material properties of surrounding connective tissue and artery walls to any other body anatomical location. Therefore, the model is not limited to the renal artery section but any other point of interest for analysis. The model also provides global variables for geometry dimensions for more straightforward adaptations to variations in anatomy.

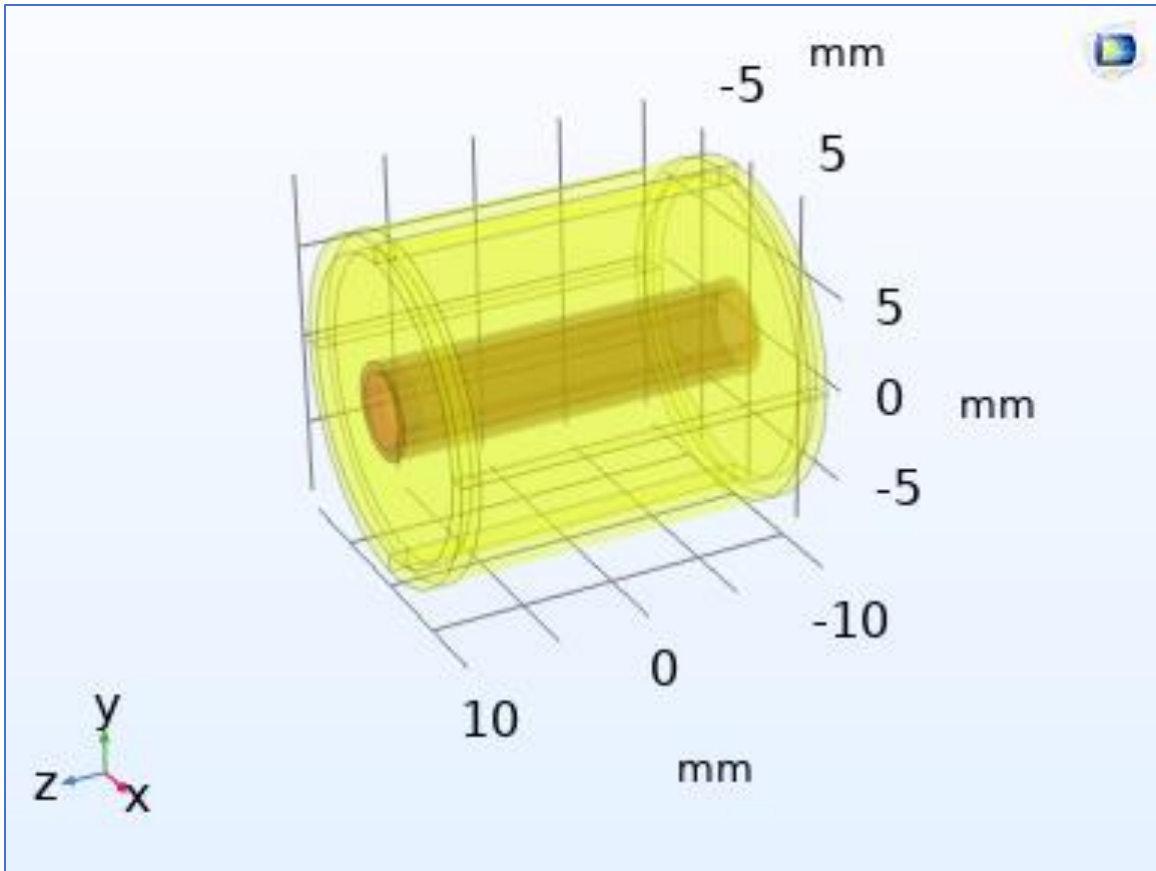


Figure 2.3 Cylindrical representation of the connective tissue surrounding the renal artery model of Fig. 2.2. Image from COMSOL Multiphysics® software.

At this point, the geometry is including the biological components of the model. The next step is to add the bipolar electrodes to the final geometry. Figure 2.4 shows the design of bipolar electrodes (patent pending) [36] with insulation over the electrodes, except for the area in electrical contact with the inside walls of the renal artery. The electrode dimensions are a diameter of 0.61 mm, length of 3 mm with a 1.5 mm separation between the electrodes. Both electrodes were assembled over another Pellethane® tube with an inner lumen carrying insulated copper wires and a Nitinol pre-shaped guide. The copper wires and Nitinol guide are not shown in Figure 2.4 or included in the simulation model since they are both covered by a perfect insulator. Since the cover is a perfect insulator, the electric fields may be quite high, but the current density is essentially zero, which means negligible heating and negligible for the simulation.

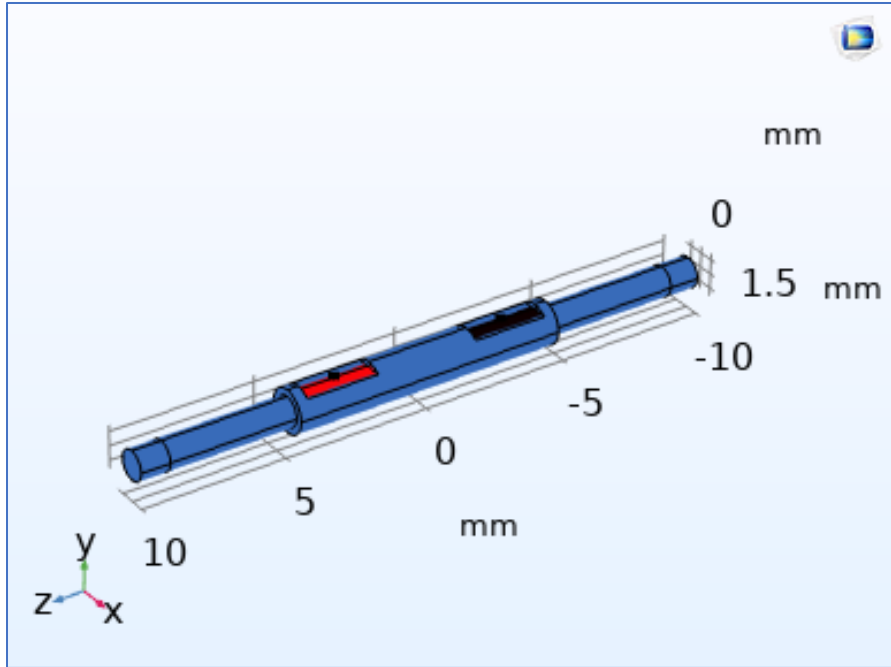


Figure 2.4 Innovative bipolar electrode design (patent pending) [36] focuses current density towards the artery wall and surrounding tissue in the renal artery. Bipolar electrodes are cylindrical rings (red and black) embedded inside a dielectric cover (blue). Image from COMSOL Multiphysics® software.

The completed geometry model is shown in Figure 2.5.

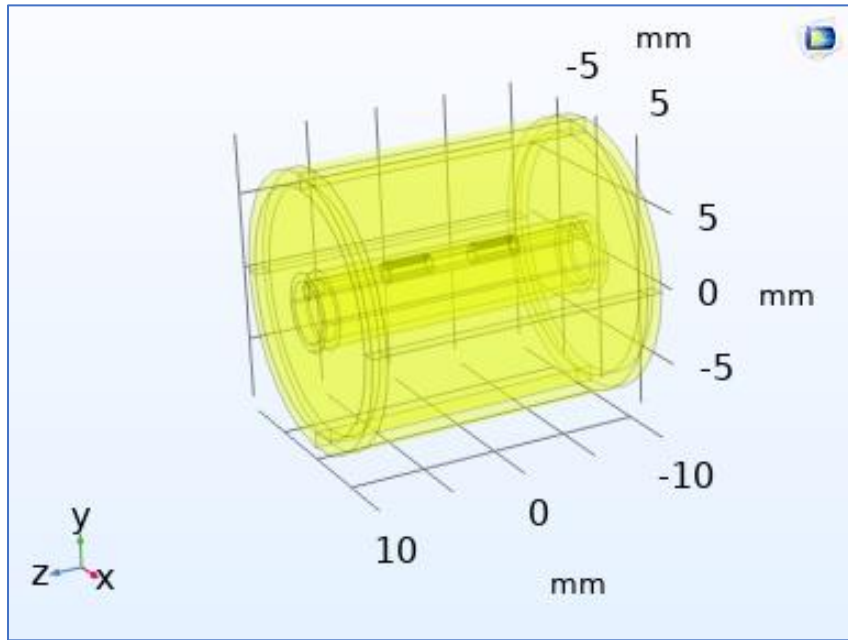


Figure 2.5 Final geometric model of the renal artery with blood, surrounding tissue, and bipolar electrodes in contact with the artery wall. Image from COMSOL Multiphysics® software.

2.2.2 Electrical and Thermal Properties of Components

The electrical and thermal properties of all the components included in the model are listed in Table 2.1, showing the material properties at 500 kHz. This data was used in the computational model to describe the blood, artery wall, connective tissue, thermoplastic catheter material (Pebax®), and electrode components. Not all properties are invariant, specifically for biological tissues which conductivity is confounded with its temperature.

Table 2.1 Electrical and thermal properties of components at 500 kHz.

Component	Electrical Conductivity σ (S/M)	Relative Permittivity (ϵ_r)	Density (kg/m ³)	Heat Capacity at Constant Pressure J/(kg-°C)	Thermal Conductivity W/(m-°C)
Blood ^a	0.748	4,190	1,050	3,617	0.52
Artery Wall ^a	0.324	312	1,102	3,306	0.46
Connective Tissue ^a	0.391	201	1,027	2,372	0.39
Pebax® 7233 ^b	1.25E-12	4	1,010	1,700	0.26
Electrodes (PtIr 90/10) ^{c,d}	1.00E+09	1	7,950	502	14

^a Dielectric Properties » IT²IS Foundation. <https://itis.swiss/virtual-population/tissue-properties/database/dielectric-properties/>

^b <https://www.materialdatacenter.com/ms/en/tradenames/Pebax/ARKEMA/Pebax%C2%AE+7233+SP+01/f21dd478/264>

^c https://www.engineersedge.com/properties_of_metals.htm

^d <https://www.azom.com/properties.aspx?ArticleID=965>

Temperature changes result in electrical conductivity changes of the biological tissues, e.g., artery walls and connective tissue. During RF ablation, tissue temperature increases through Joules heating; therefore, the need to include in the FEM model the relationship between variations to the electrical conductivity for both tissues. Experimental data established the linear relationship with the equation [40]

$$\sigma(T) = \sigma_0[1 + k_1\Delta T] \quad (1)$$

where σ_0 is the initial electrical conductivity at the reference temperature, k_1 is the temperature coefficient, and ΔT [°C] is the temperature difference from the initial reference temperature. Set $k_1 = 2.05\%/^{\circ}\text{C}$ per empirical data, and the linear electrical conductivity in the model for artery is

$$\sigma(T) = 0.324[1 + 0.0205\Delta T] \quad (2)$$

Consequently, the linear electrical conductivity equation for connective tissue was

$$\sigma(T) = 0.391[1 + 0.0205\Delta T] \quad (3)$$

Both equations (2) and (3) are bounded within the experimental data of 30 to 80°C as a conservative approach since the scope of this research is to design an ablation system with low power to induced “slow targeted ablation” and prevent reaching high temperature. Furthermore, conductivity drops sharply at 100°C since the charring of tissue results in evaporation of liquids and conductive media [41], which is not desirable for this application.

The electrical and thermal properties of all the components listed in Table 2.1 were configured in the materials module of the COMSOL Multiphysics® model. In addition, the conductivity dependence with temperature in equations (2) and (3) was included in the model as piecewise functions that adjusted the biological tissue conductivity with its transient temperature and bounded to the experimental data limits.

2.2.3 Electric Field

RF ablation is a technique used to create a hyperthermic zone between two electrodes and induce denaturation of cells or ablation. The physic that explains RF ablation is Joule heating, where the goal is to raise the tissue temperature between the electrodes to 60°C or greater [37] with radiofrequency. First, the Electric Currents frequency domain module in COMSOL Multiphysics® is used to solve the spatial vectors of electric field and current density. Then the numerical solution is coupled with the heat transfer module to determine the transient Joule heating power dissipated inside the tissue, resulting in tissue ablation.

The electrical signal applied between the electrodes is AC vs. DC to prevent neurostimulation and pain to the patient. Typical medical equipment in the operating room operates at 500 kHz since nerve stimulation occurs at frequencies below 10 kHz [37]. Broadly, an

RF ablation system consists of a signal generator, an electrode, electrode return pads, and cables connecting these elements [37]. The electrode is in contact with the targeted tissue, and the return ground pad (or surface dispersive electrode) [39] is larger than the electrode in contact with the outer skin. Since energy flows between the electrodes, it is not only the ablation electrode that increases temperature but also the return ground pad. There is a complication to this design when the ground pad is not in complete contact with the skin. If improper contact or partial ground pad is performed, the current densities will increase in the contact areas resulting in higher temperatures. Undesirable and dangerous skin burns could result and have been reported when using ground pads [37] [38] [39]. The design in this research does not require a grounding pad since the design is a bipolar electrode within the artery. The Joule heating temperature rise and ablation will intentionally occur over both electrodes; therefore, this design eliminates the risk of skin burns.

When electric fields are applied to tissue, the temperature in the zone between the bipolar electrodes increases due to Joule heating through tissue conduction and dielectric losses. Therefore, an examination of the electrical properties of the components in the model is performed to determine how these materials behave at a RF signal of 500 kHz and determine if the magnetic fields and heating due to induced currents (in addition to Joule heating) must be included in the model [42]. Table 2.2 shows the electrical conductivity, relative permittivity, skin depth, and complex conductivity for each component at 500 kHz.

First, a comparison of the model maximum dimensions and the RF signal wavelength demonstrates that induced currents are negligible. The model's maximum dimensions are 20 mm X 20 mm X 20 mm. The RF signal of 500kHz has a wavelength of 599.58m as calculated by

$$\lambda = \frac{f}{c} \text{ (m)} \quad (4)$$

where λ (lambda) is the wavelength in meters, c = speed of light ($3.0E+8$ m/s), and f = frequency in Hz. Since the wavelength of the ablation frequency (~ 600 m) is much greater than the model (20 mm), this is a quasi-static analysis, and the AC/DC module of COMSOL Multiphysics® is appropriate for the simulation.

Next is the calculation of the skin depth for the 500 kHz signal in all the components of the model. Utilizing the conductivity (σ) and relative permittivity (ϵ_r) from Table 2.1, the skin depth (δ) and complex conductivity ($\sigma + j\omega\epsilon_0\epsilon_r$) is calculated to determine if induced currents should be included in the model for any component. Skin depth (δ) is calculated with the formula [46]

$$\delta = \frac{1}{\sqrt{\pi f \mu \sigma}} \text{ (m)} \quad (5)$$

where $\pi = 3.14$, $f = 500\text{kHz}$, $\mu \sim \mu_0 = 4\pi E-07$ is the permeability of the components which is approximate to free space and σ for each component is listed in Table 2.1. The complex conductivity is calculated by [46]

$$\sigma + j\omega\epsilon_0\epsilon_r \text{ (S/m)} \quad (6)$$

where σ and ϵ_r are obtained from Table 2.1, $\epsilon_0 = 8.854E-12$ (farads/m) is the permittivity of free space and ω is the angular frequency of the RF signal, which is calculated by

$$\omega = 2\pi f \text{ (rad/s)} \quad (7)$$

where $f = 500$ kHz is the frequency of the RF ablation signal applied in the model [46].

Table 2.2 Skin depth and complex conductivity of components at 500 kHz.

Component	Electrical Conductivity σ (S/m)	Relative Permittivity (ϵ_r)	Skin Depth δ (m)	Complex Conductivity $\sigma + j\omega\epsilon_0\epsilon_r$ (S/m)
Blood	0.748	4,190	0.823	0.748 + j 1.17E-01
Artery Wall	0.324	312	1.250	0.324 + j 8.68E-03
Connective Tissue	0.391	201	1.138	0.391 + j 5.59E-03
Pebax® 7233	1.25E-12	4	6.37E+05	1.25E-12 + j 1.11E-04
Electrodes (PtIr 90/10)	1.00E+09	1	2.25E-05	1.00E+09 + j 2.78E-05

From Table 2.2, it can be observed that the skin depth of blood, artery wall, and connective tissue (from 0.82 to 1.25 m) and the overall model dimension of the model (20 mm) are significantly smaller than the wavelength of the RF (600 m) signal.

The complex conductivity of non-biological materials (Pebax® 7233 and electrodes) has a real component of more than eight orders of magnitude compared to the imaginary component. Finally, the Pebax® 7233 has a nearly zero conductivity, and the electrodes have nine orders of magnitude in conductivity, making them a perfect insulator and a perfect conductor, respectively.

In conclusion, heating due to induced currents from magnetic fields is negligible. Therefore, it does not need to be included in the model resulting in a simplified solution of static field without risking accuracy on results for the scope of this research.

In resistive media, the relationship between current and electric field is established by equation [46]

$$\mathbf{J} = \sigma \mathbf{E} \text{ (A/m}^2\text{)} \quad (8)$$

where \mathbf{J} is current density, σ is conductivity (S/m), and \mathbf{E} is the electric field (V/m). For static fields and stationary current, continuity requires the net flow of current in the model to be zero, therefore

$$\nabla \cdot \mathbf{J} = 0 \quad (9)$$

Substituting (8) into (9) results in equation

$$\nabla \cdot \sigma \mathbf{E} = 0 \quad (10)$$

Equation (10) can be expanded to

$$\nabla \cdot [(\sigma + j\omega \epsilon_o \epsilon_r)] \nabla V = 0 \quad (11)$$

The electric field \mathbf{E} (V/m) is calculated from the negative gradient of the voltage applied using equation

$$\mathbf{E} = -\nabla V \text{ (V/m)} \quad (12)$$

which turns the scalar voltage V (V) into a vector field. Next, the current density \mathbf{J} (A/m²) is calculated from

$$\mathbf{J} = \frac{\mathbf{E}}{\rho_\varepsilon} \text{ (A/m}^2\text{)} \quad (13)$$

where ρ_ε is the electrical resistivity of the material ($\Omega\cdot\text{m}$). Lastly, the average power dissipated in the tissue due to Joule heating between the electrodes is calculated by

$$P_{\text{av}} = \frac{1}{2} \Re(\mathbf{J}^* \cdot \mathbf{E}) \text{ (W/m}^2\text{)} \quad (14)$$

where \Re is the real part from the vector dot product of the complex conjugate of \mathbf{J} and \mathbf{E} .

Now that the electrical model is defined, the next step is to define the thermal model.

2.2.4 Bioheat Equation

The objective of the thermal model is to compute the transient temperature distribution within the tissue resulting from the electrical heating of the RF signal and predict the size of the ablated zone. The governing equation for temperature is the Pennes Bioheat which describes the temperature distribution surrounding the bipolar electrodes during Joule heating and incorporates the convective heat transfer from blood perfusion within the tissue. The Pennes bioheat equation

$$\rho C_p \frac{\partial T}{\partial t} - \nabla \cdot k \nabla T = \frac{1}{2} \Re(\mathbf{J}^* \cdot \mathbf{E}) + \rho_b C_{p,b} \omega_b (T_b - T) + Q_{\text{met}} \quad (15)$$

use the power dissipated by Joule heating (14) to calculate temperature (T), where ρ is the tissue density (kg/m³), C_p is the tissue-specific heat (J/kg·K), and k is the tissue thermal conductivity (W/m·K). T_b is the blood temperature (assumed to be 37°C), ρ_b is blood density (kg/m³), $C_{p,b}$ the specific heat of blood (J/kg·K), and ω_b is the blood perfusion (1/s). Q_{met} is the energy generated by metabolic processes (W/m³) within the blood. It is negligible for this model since there is no significant source of metabolic energy within the blood at normal body temperature (37°C) compared to the energy generated from Joule heating (>60°C) in this specific model.

Resistive heating produces Joule heating between ions (Na, K, Cl) present inside the tissue induced by the RF signal applied between the electrodes. Heat is also spread by thermal conduction to nearby tissue while the signal is applied, resulting in spatial thermal ablation when the temperature equals or exceeds 60°C. The ablation zone is determined by temperature, time, and the design of the electrodes. Additional factors influencing the ablation zone include tissue electrical and thermal properties. The higher the ablation temperature, the faster ablation is achieved; however, exceeding 100 °C causes tissue charring and vaporization, resulting in reduced heating [37] [38] [39]. After electrical and thermal model definition are the boundary conditions.

2.2.5 Boundary Conditions

The bipolar electrodes are made of Platinum Iridium and are considered perfect conductors. Based on their conductivity values in Table 2.2, it is unnecessary to define those domains in the model since its surfaces are equipotential. Furthermore, the RF signal wavelength is much larger than the model established in section 2.2.3 of electric fields. The terminal boundary condition was used in the AC/DC module of COMSOL Multiphysics® to fix the RF signal on all the electrode surfaces. Although there should exist finite heat loss within the electrode itself, it is many orders of magnitude lower than in the ablated tissue. Even though the current density on the conductor surface can be high, specifically near borders with small areas, the electric field along the surface of the electrode is negligible since the voltage over the perfect electrode conductors is considered relatively constant.

Similarly, since the insulators are essentially perfect, these domains can also be eliminated from the electrical model. In the insulators, the electric fields may be quite high, but the current is essentially zero, which means negligible heating. The electric insulation boundary condition can

be applied to the insulators' boundaries and implies no current (neither conduction nor displacement currents) passes through these boundaries.

The remaining biological components of artery walls and connective tissue are assigned the Dirichlet boundary conditions of initial temperature equal to normal body temperature (37°C) and initial voltage = 0 V.

2.2.6 Ablated Tissue Definition

To determine the ablation zone (i.e., where cell death occurs), the Thermal Damage transformation module was added to the model with a temperature threshold defined in Table 2.3. The isothermal surfaces were plotted using the following parameters to determine the ablation zone: damage temperature 60°C, damage time 1 s, necrosis temperature 90°C (reduced from 100°C as a safety factor). The enthalpy change defines the enthalpy variation within the tissue that occurs during the ablation process. A thermodynamic quantity is equivalent to a system's total heat content. The enthalpy change is set to 0 J/kg for this model since the internal energy of the system plus the product of pressure and volume are constant.

Table 2.3 Thermal tissue damage threshold parameters.^a

Parameter	Value
Damage temperature	60°C
Damage time	1 s
Necrosis temperature	90°C
Enthalpy change	0 J/Kg

^a Thermal damage option in Bioheat transfer module of COMSOL v5.6

2.2.7 Computational Model Summary

The complete model of the renal artery with bipolar electrodes combines a frequency-domain electromagnetic analysis with a transient bio-thermal system. COMSOL Multiphysics® solves this coupled model using the frequency-transient study type. The frequency-domain problem is a stationary linear equation since the electrical properties are linear with respect to

electric field strength over one period of oscillation. Thus, COMSOL Multiphysics® first solves the voltage field using a stationary solver and then computes the resistive heating. This resistive heating term is then passed over to the transient thermal problem, which is solved with a time-dependent solver. Finally, this solver computes the change in temperature over time.

The frequency-transient study type automatically accounts for material properties that change with temperature and the tissue damage fraction. For example, suppose the temperature rises or tissue damage causes the material properties to change sufficiently to alter the magnitude of the resistive heating. In that case, the electrical problem is automatically recomputed with updated material properties.

2.3 Numerical Simulation Results

The model is finalized in COMSOL by configuring the Multiphysics® module, which transfers the current density solution in space and time to the bioheat module and calculates the transient heat transfer with the resulting temperature spatial distribution. Finally, a predefined “fine” mesh is implemented with a combination of Free Tetrahedral in the ablation zone and a final swept of major geometries on the surrounding areas of the model.

Figure 2.6 shows the numerical solution of the electrical field generated from an applied signal of 500 kHz and 60 Vp-p after 60 seconds. Note that the positive electrode (red) is at 60 V, and the negative electrode (blue) is at 0V as a bipolar electrode. The scalar voltage distribution is represented with colors from 60V with red and transitioning into 0V with the blue color. Observe that voltage around the electrodes is primarily green, representing 30V. The current density from the bipolar electrodes through the surrounding tissue is represented with red arrows with proportional magnitudes. Note that current density flows only through the exposed surfaces of the bipolar electrodes from the positive (red) to the negative (blue) electrode. Even though the

electrodes are cylindrical shapes, the dielectric cover allows only contact with renal artery walls through a prefabricated window.

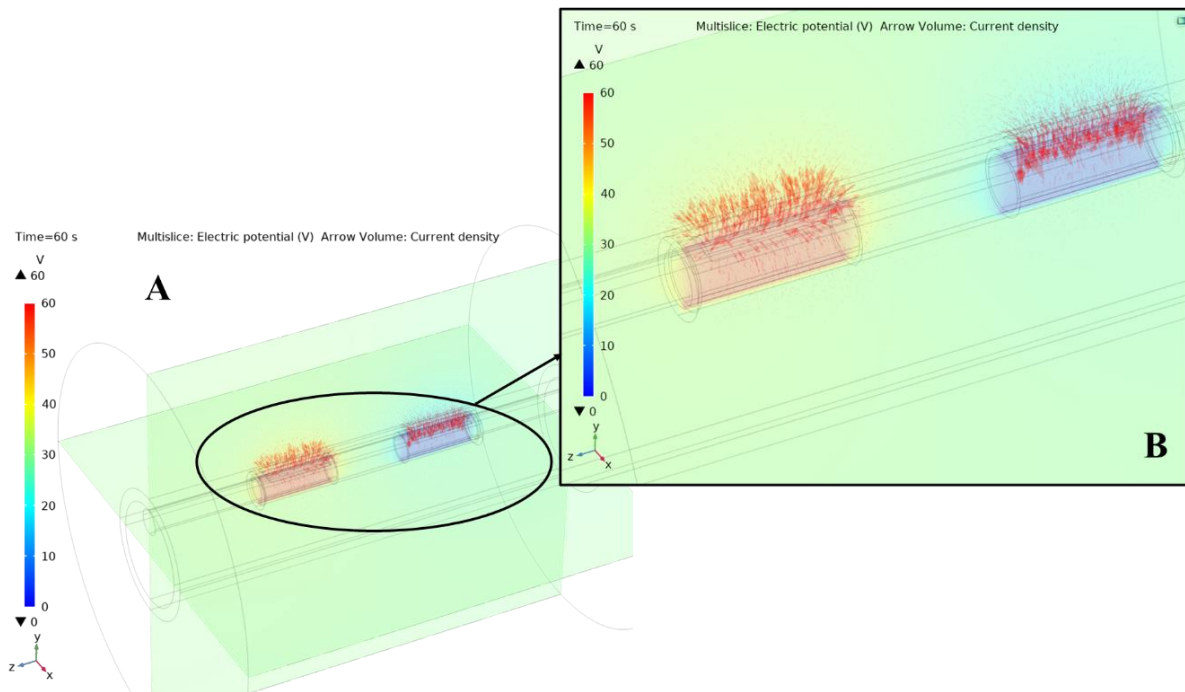


Figure 2.6 Numerical solution of model with 60 Vp-p and current density with bipolar electrodes. (A) Voltage field from 60V to 0V distributed between bipolar electrodes. (B) Zoom in to bipolar electrodes' exposed surface and current density flowing from positive to the negative electrode and through exposed surfaces.

Figure 2.7 shows the isothermal surfaces from the numerical solution. The surrounding temperature is at 36.7°C confirming the boundary condition of normal body temperature as the baseline. The maximum temperature achieved is 88°C and is located near the electrode surfaces and extends through convection through the surrounding tissue between the electrodes. The current flows mainly from the positive to the electrode producing Joules heating and raising the temperature. With 60 seconds of exposure, the temperature between the electrodes reaches equilibrium and stops increasing. The temperature was maintained well 12°C below 100°C to prevent reaching tissue charring and vaporization, which is not desirable for the ablation.

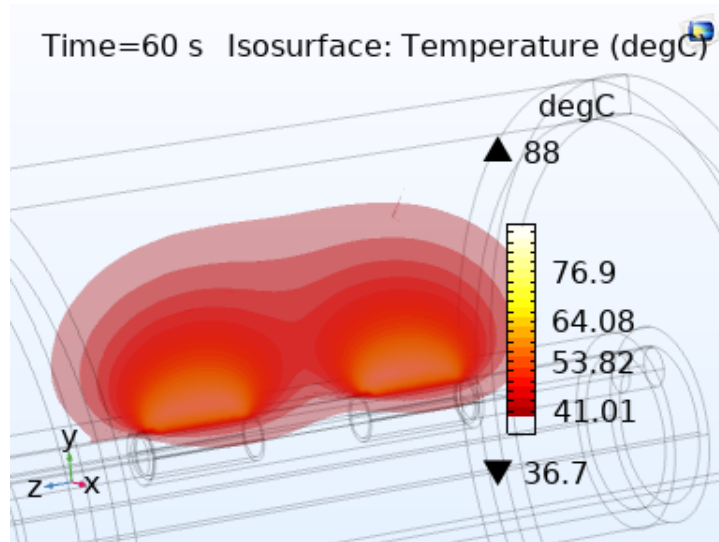


Figure 2.7 Numerical solution of model showing in the isothermal surface graphic the ablated surrounding tissue heated to more than 60°C and less than 90°C.

Figure 2.8 shows the isothermal surfaces from Figure 2.7 but filtered only for the effective ablation temperature between 60°C and 90°C as stated in this research scope). The ablation zone is observed as two separate lobe shape zones above the electrodes. The ablation zone measured from the numerical model in Figure 2.9 and Figure 2.10 is 2.1 mm (W) x 9.0 mm (L) x 1.7 mm (H) after 60 seconds of continuous application of the ablation signal.

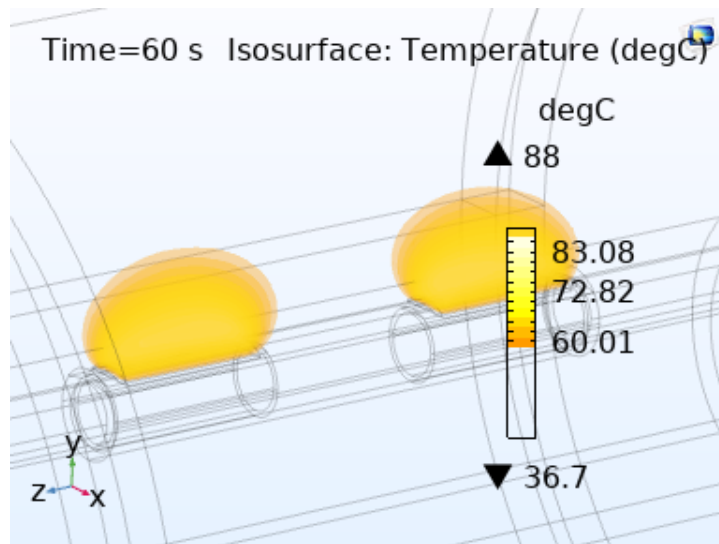


Figure 2.8 Isothermal surfaces filtered for the effective ablation temperature of 60°C and 90°C. The ablation zone is observed as a two-lobe shape zone above the electrodes.

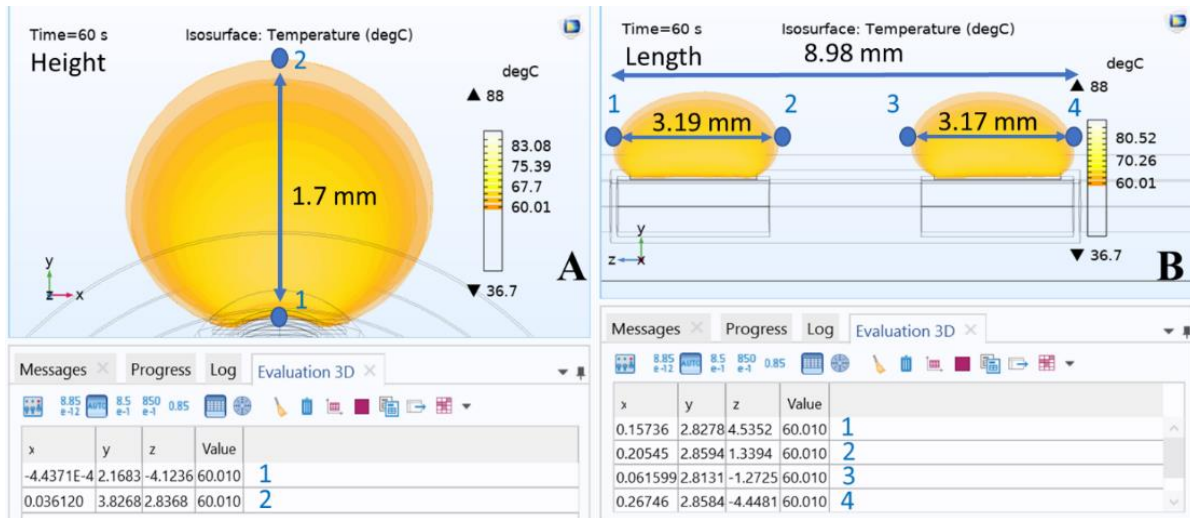


Figure 2.9 Height and length dimensional measurements of the ablation zone from the numerical model after 60 seconds of ablation. (A) Overall height is 1.7 mm of both lobes. (B) The overall length of both lobes is 8.98 mm, with lobe over positive electrode is 3.19 mm long and lobe over the negative electrode is 3.17 mm long.

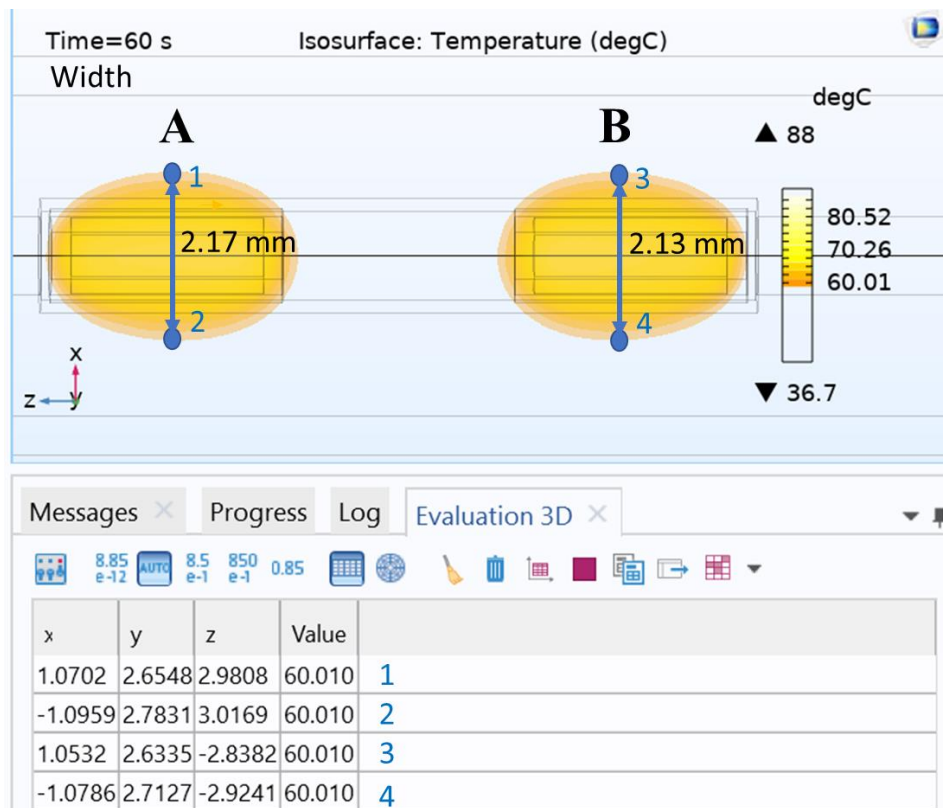


Figure 2.10 Width dimensional measurements of the ablation zone from the numerical model after 60 seconds of ablation. (A) ablated zone over the positive electrode is 2.17 mm wide and (B) ablated zone over the negative electrode is 2.13 mm wide.

2.4 RF Ablation Catheter Design and Build

The innovative design of bipolar electrodes (patent pending) [36] shown in Figure 2.4 resulted from multiple computer simulations of the model. Adjustments to the electrode dimensions and separation between them were the two critical variables to maximize the ablation zone with the minimum power requirements. The optimum bipolar design resulted in an electrode diameter of 0.61 mm, length of 3 mm with a 1.5 mm separation between the electrodes. Thus, voltage and time are the remaining variables to adjust for the desire ablation zone.

Once the bipolar electrode design was optimized, it was assembled in a basket catheter for deployment into a renal artery with the assistance of a commercially available guiding sheath as in Figure 1.4. The bipolar electrode design in this study was assembled in a 6 Fr (1Fr = 1/3 mm) [43] catheter with four collapsible splines carrying either 2 or 4 electrodes each. Each spline is made of thermoplastic (Pebax®) extrusions with their inner lumen containing a pre-shaped nickel-titanium (Nitinol) and electrical wires, as shown in Figure 2.11. Nitinol provides a flexible and collapsible basket shape that can be delivered through femoral access into the renal artery. It expands to the pre-shaped form creating firm connectivity between the electrodes and the artery inner walls. Each bipolar electrode can be independently selected for ablation at each quadrant in contact with the splines inside the artery (patent pending) [36].

Detail build description of the catheter follows from inner to outer components assembly starting with the electrodes. Each electrode is laser welded to an AWG44 nickel wire insulated with poly/nylon. Then, each electrode and wire assembly are threaded through Pebax 7233 extrusion tubing with 40% BaSO₄ for positioning during fluoroscopy. The electrodes are positioned at the designed dimensions from the FEM model. Each tubing dimension is 0.46 mm outside diameter, 0.13 mm thickness, 20 mm long. Each tubing assembly with electrodes and wires

is threaded through the inner lumen with a pre-shaped Nitinol wire with 0.356 mm outside diameter and 20 mm long. The electrodes are covered with another Pebax 7233 extrusion tubing with exposure windows fixed in place with cyanoacrylate. Each assembled spline can accommodate two to four electrodes. Finally, each assembled spline is held in place at 120 degrees from the other with a plastic coupler machined to hold each spline in alignment. The splines can move freely from a pre-shape form as in Figure 2.11 A to a collapsed shape in compliance with the renal artery inside diameter, as shown in Figure 2.11 B. A center polyamide shaft serves as a guide to help the splines movement during deployment through a guided sheath into the femoral access.

All nickel wires are threaded through another 6Fr sheath and sealed at both ends to prevent blood ingress during the procedure. The proximal end of the sheath will end at a standard electrical connector for interface with an external generator or a monitoring device.

A completed basket catheter for RF ablation of renal nerves can be easily deployed through a guiding sheath for positioning inside the renal artery under fluoroscopy.

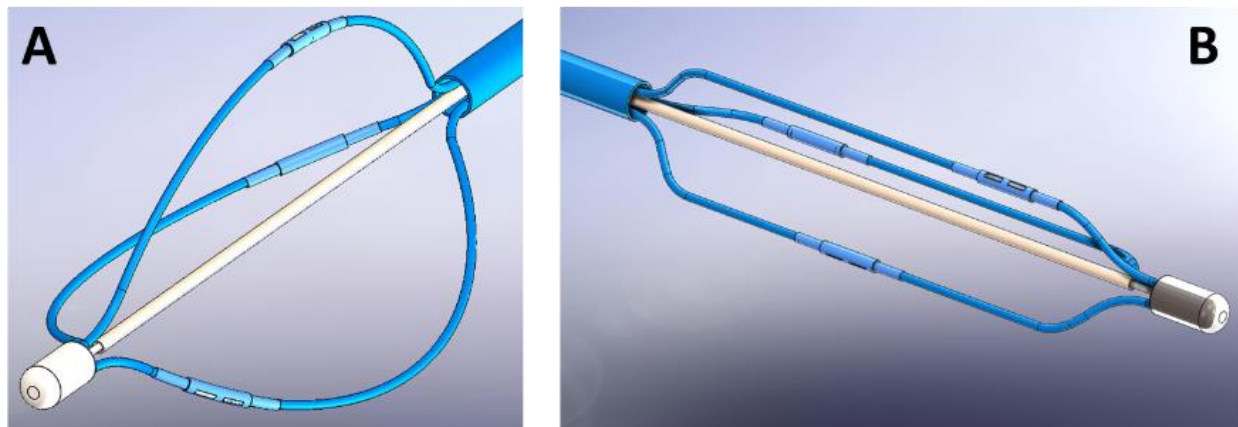


Figure 2.11 Graphical representation of the basket catheter with three splines and two electrodes per spline. (A) Basket deployed in an unrestrained open space showing Nitinol pre-shaped form covered by blue Pebax®. (B) Basket deployed inside a constraint space, such as an artery. Note the electrodes are not in the same circumferential plane to prevent renal artery stenosis after ablation.

2.5 Summary

A computational model of the renal artery system with a bipolar RF ablation was developed using COMSOL Multiphysics® software. The model includes electrical and thermal properties of artery walls, surrounding connective tissue, and electrodes. In addition, a frequency-domain electromagnetic analysis with a transient bio-thermal system was coupled with a frequency-transient study which automatically accounts for conductivity changes with temperature and the tissue damage fraction.

The applied signal of 500 kHz and 60 Vp-p was simulated for 60 seconds while in electrical contact with the biological tissue. The simulation showed current density flowing between the bipolar electrodes only through the exposed surface of the electrodes. The ablated tissue was defined in the model as the volume with an induced temperature between 60°C to 90°C. The predicted ablation zone, as shown in Figures 2.9 and 2.10, measured overall 2.1 mm (W) x 9.0 mm (L) x 1.7 mm (H). The ablated tissue, specifically over each of the bipolar electrodes, formed a lobe shape zone that measured lengths of 3.19 mm over the positive electrode and 3.17 mm over the negative electrode. The width measured 2.17 mm and 2.13 mm over the positive and negative electrodes, respectively. The height was similar on both with 1.7 mm.

The model provided a fast method to perform iterations for design improvements of the bipolar electrodes. Multiple iterations in electrode dimensions, separation, and exposed surface resulted in an optimized design that maximized the ablation zone with the shortest time and power.

The model also demonstrated that RF ablation is possible with bipolar electrodes without the need for a return ground pad, which is commonly used in commercially available unipolar ablation catheters and generators. Furthermore, the bipolar electrodes were assembled over Pebax®, which serve as an excellent dielectric to contain a pre-shaped nitinol wire for further

development during this investigation. The nitinol will serve to form the shape of a basket catheter and eliminate the need for a balloon to provide support to the electrode and maintain electrical contact with the ablated tissue.

Therefore, this research designed a bipolar device that eliminates the need for a ground pad and the risk of unwanted skin burns by focusing the energy on the ablation zone. In addition, the electrode dimensions provide a localized, targeted ablation zone requiring lower power requirements compared to conventional commercialized devices. Additionally, the electrodes are strategically assembled in different circumferential planes at the right angle from the catheter shaft to prevent renal artery stenosis after ablation [20].

Next, a method for testing the bipolar model for RF ablation is required with similar agility and speed as the FEM modeling developed. The intention is to leverage *in silico* and *in vitro* experiments to provide an efficient platform for design improvements and iterations.

The *in vitro* alternative shall provide a quick and cost-effective method to perform RF ablations to quickly visualize the ablated zone's geometry. In addition, a phantom tissue capable of permanently changing color is ideal for testing the prototype and returning to the numerical model for further design iteration improvements.

Chapter 3: *In Vitro* Tissue Phantom Experiments

3.1 Thermochromic Phantom (TCP) Tissue

Testing RF ablation devices requires *ex vivo* tissue to confirm its functionality per design before moving into *in vivo* testing and, eventually, human trials. The traditional approach requires multiple iterations where a new tissue was utilized for every trial. This process is time-consuming and demands new *ex vivo* samples for each test iteration, and, still, predicting performance *in vivo* is uncertain. With the numerical simulation (*in silico*) and modeling approach, the need for *ex vivo* tissue trials is reduced significantly. Multiple design iterations can be performed first via numerical simulation, then validated with *ex vivo* tests resulting in a faster, more efficient, and nature-conscious design optimization process. Once the design is optimized to the expected level, an *ex vivo* test can follow a higher degree of predictability than the traditional approach.

Further reduction of *ex vivo* tissues during numerical model, e.g., *in silico*, validation, and design iterations, is achieved using a thermochromic phantom (TCP) tissue in an *in vitro* setup. The TCP is formulated with similar electrical properties as the targeted tissue providing a fast and straightforward medium for testing. An *in silico* and *in vitro* combination provides the most efficient process to perform design iterations resulting in higher design predictability with higher confidence for moving into *ex vivo* tissue tests and, ultimately, *in vivo*.

This research utilized TCP tissue to perform *in vitro* tests for direct visualization of the ablation zone and measured dimensions to validate the *in silico* results. The three-dimensional (3D) isothermal contour graphics available in COMSOL Multiphysics® software [33] provided a

comparison framework for validating the *in silico* results with the *in vitro* TCP tissue thermal visualization measurements. The TCP tissue mimicked the *ex vivo* tissue. In addition, it was developed with equivalent electrical properties resulting in a more efficient alternative through a significant reduction of design iterations during this research. The TCP was prepared using polyacrylamide gel with a thermochromic ink additive that permanently changes color from base (off-white) color to magenta when heated over 60°C [44]. Figure 3.1 shows the color characterization chart for the TCP when subjected to temperature changes. This chart serves as the standard to compare the *in vitro* tests with the *in silico* numerical results from the model.

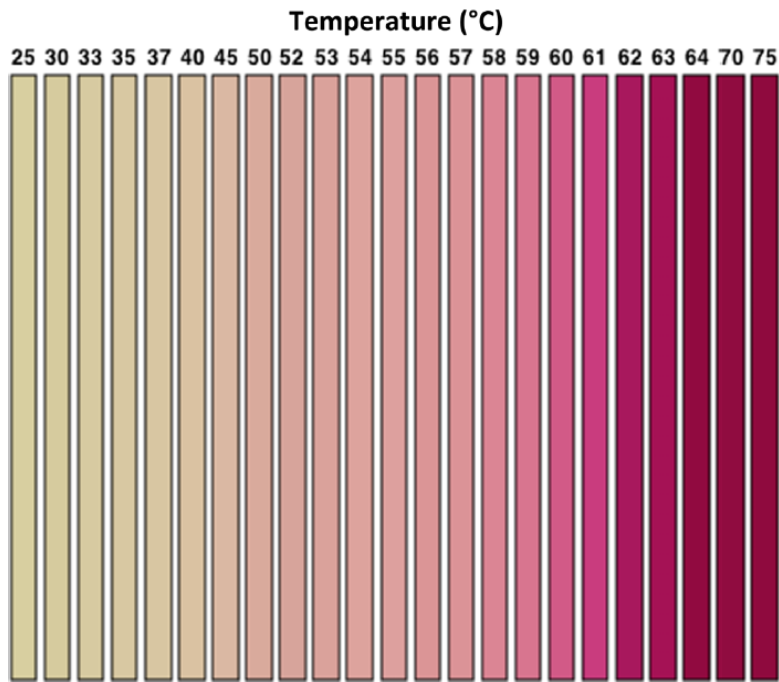


Figure 3.1 Color chart of TCP tissue for temperatures between 25°C and 75°C. Note. From [44]. © J. Wiley. Used with permission.

3.2 TCP Tissue Formulation and Preparation

The TCP was formulated as described by Mikhail *et al.*, [44], and individual components are summarized in Table 3.1. In addition, the electrical conductivity was adjusted to match the

average between the renal artery and connective tissue conductance in Table 2.1 since this is the most relevant parameter relating to the thermal Joule heating effect.

Table 3.1 Thermochromic phantom tissue recipe.

Component	Proportion
Deionized water	76.1 (v/v)
40% acrylamide/bis-acrylamide	17.5 (v/v)
Magenta MB60°C concentrate	5.0 (v/v)
Sodium chloride (NaCl)	0.9 (w/v)
Ammonium Persulfate (APS)	0.14 (w/v)
N, N, N', N'-tetramethylethylenediamine (TEMED)	0.14 (v/v)

3.3 Radiofrequency Ablation of TCP Tissue

TCP samples were prepared and ablated with a bipolar electrode connected to a waveform generator and linear amplifier, as shown in Figure 3.2. A simplified one-line diagram is shown in Figure 3.3 (oscilloscope and precision meter not shown for clarity) to document the laboratory setup. The exposed surface of the electrodes (from Figure 2.4) was placed over the TCP in electrical contact, as shown in Figure 3.3 (D). Both electrodes and TCP setup were impregnated with saline solution adjusted to the conductivity of blood as listed in Table 2.1. An insulation plate was placed over the bipolar electrode and TCP to maintain electrical contact during the ablation. Then, an ablation signal of 3.0 Vp-p and 500 kHz was applied with an Agilent 33220A waveform generator (Agilent, Santa Clara, CA, USA) and amplified to 60 Vp-p with a Pendulum F20A fixed-gain linear amplifier (Pendulum, Stockholm, Sweden). A Tektronix TDS2001C oscilloscope (Tektronix, Beaverton, OR, USA) and a Fluke 8846A Precision Multimeter (Fortive, Everett, WA, USA) were connected to monitor and confirm that the appropriate ablation signal was applied to the TCP through the electrodes. This setup was maintained and video recorded during each TCP ablation iteration.

During the multiple iterations, valuable knowledge was obtained on methods to achieve the expected RF ablation. This knowledge improved the bipolar design electrodes, leading to a filing for patent [36].

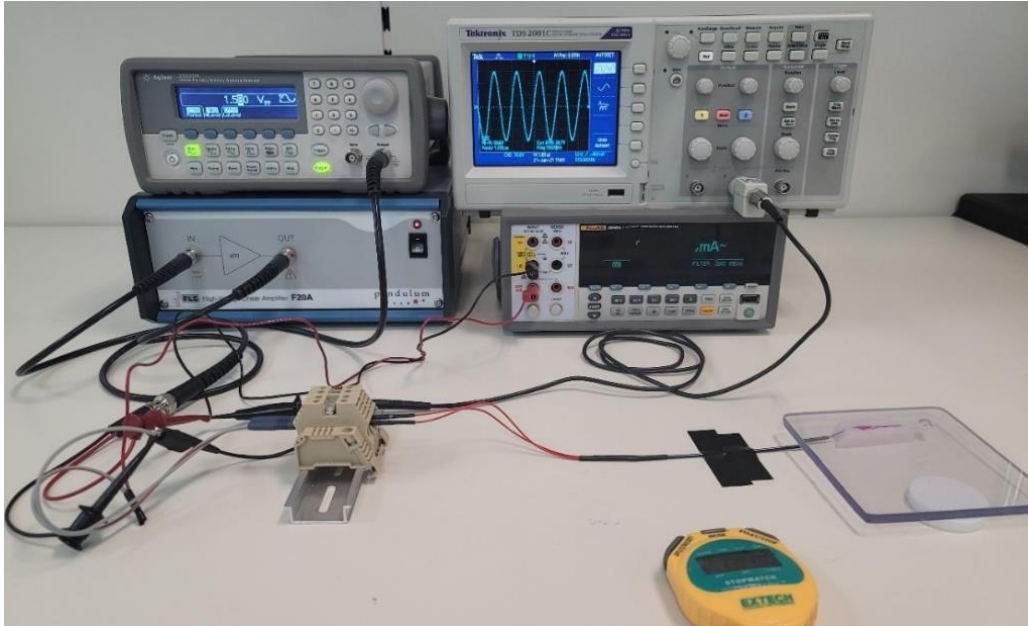


Figure 3.2 *In vitro* setup for the ablation of Thermochromic phantom (TCP) tissue.

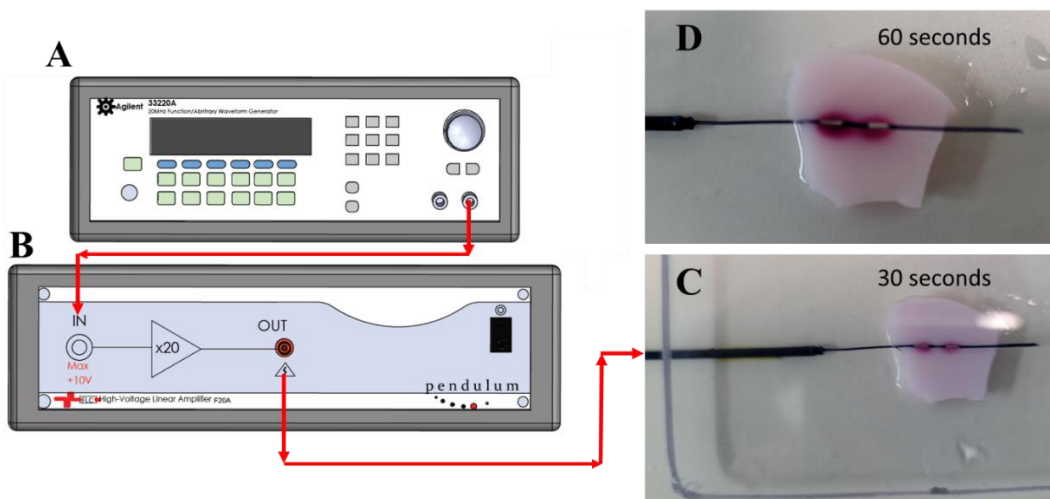


Figure 3.3 Simplified diagram of the *in vitro* setup for the ablation of the Thermochromic phantom (TCP) tissue. (A) Signal generator (3 Vp-p, 500 kHz) was amplified by (B) 20x gain linear power amplifier (60 Vp-p, 500 kHz) and (C) applied to TCP with a bipolar electrode and an insulating plate to maintain its position at 30 seconds (D) TCP ablation at 60 seconds. Oscilloscope and precision meter not shown for clarity.

3.4 Determination of TCP Tissue Ablation Zone

The ablated TCP tissue was removed from the electrode and its dimensions measured. Length (L) and width (W) were measured first, and then the height was measured last since it was a destructive measurement that required the phantom to be sliced with a scalpel. Next, the TCP was sliced through the center to measure the height (H) of the ablated zone. Using the color chart in Figure 3.1 for color indicating $\geq 60^{\circ}\text{C}$ and compared to the TCP tissue, the estimated ablation zone overall dimensions are approximately 2 mm (W) x 9 mm (L) x 2 mm (H) as shown in Figure 3.4 (A) (B) (C). From Figure 3.4 (D), the dimensions of the lobes over the electrodes are 3 mm approximately for both positive and negative. The positive lobe is identified with the most intense magenta color on the TCP tissue.

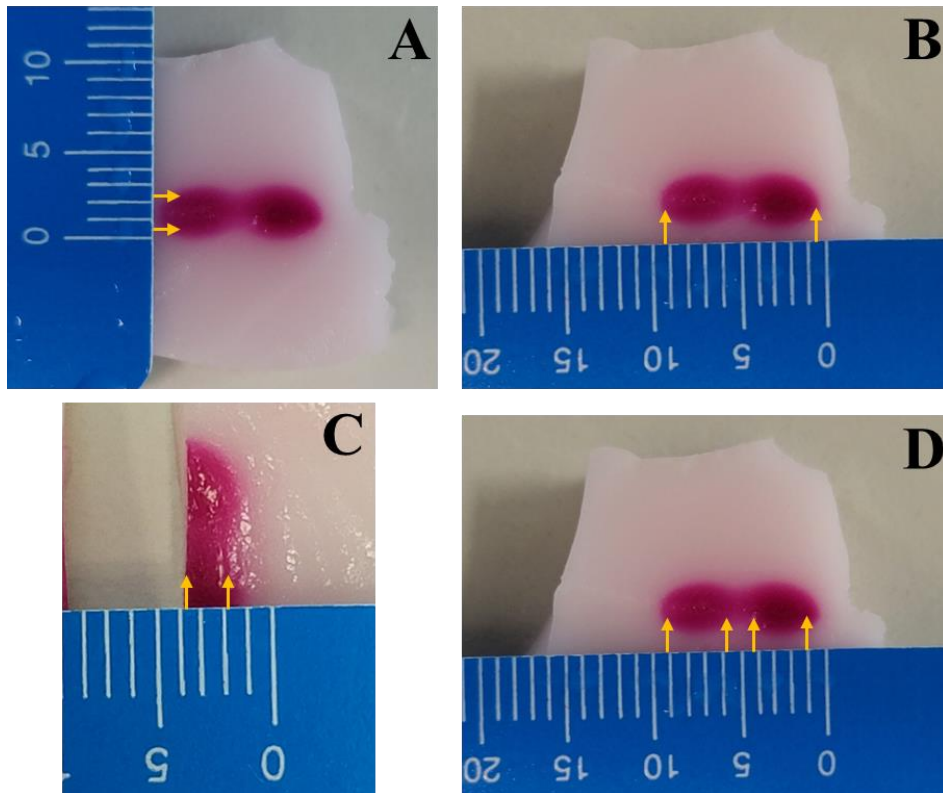


Figure 3.4 Bipolar ablation zone of TCP tissue with the temperature reaching $\geq 60^{\circ}\text{C}$ is approximately (A) 2 mm (W) x (B) 9 mm (L) x (C) 2 mm (H). Each ablated lobe shape (D) is approximately 3 mm. Temperature reference for the 60°C color chart is used from Figure 2.12 and approximated to the highest intensity observed to be $\geq 60^{\circ}\text{C}$.

3.5 Comparison Between *In Silico* and *In Vitro* Results

Visualization of the thermal distributions between *in silico* and *in vitro results* are placed side by side for comparison in Figure 3.5. The numerical model prediction of temperature rise, ablation zone geometry, and location correlate closely with the TCP tissue thermal zone resulting from the *in vitro* experiments. The isothermal scale of the model was adjusted to a minimum of ~45°C to match the start of color change in the TCP tissue with temperature as per the color chart in Figure 3.1.

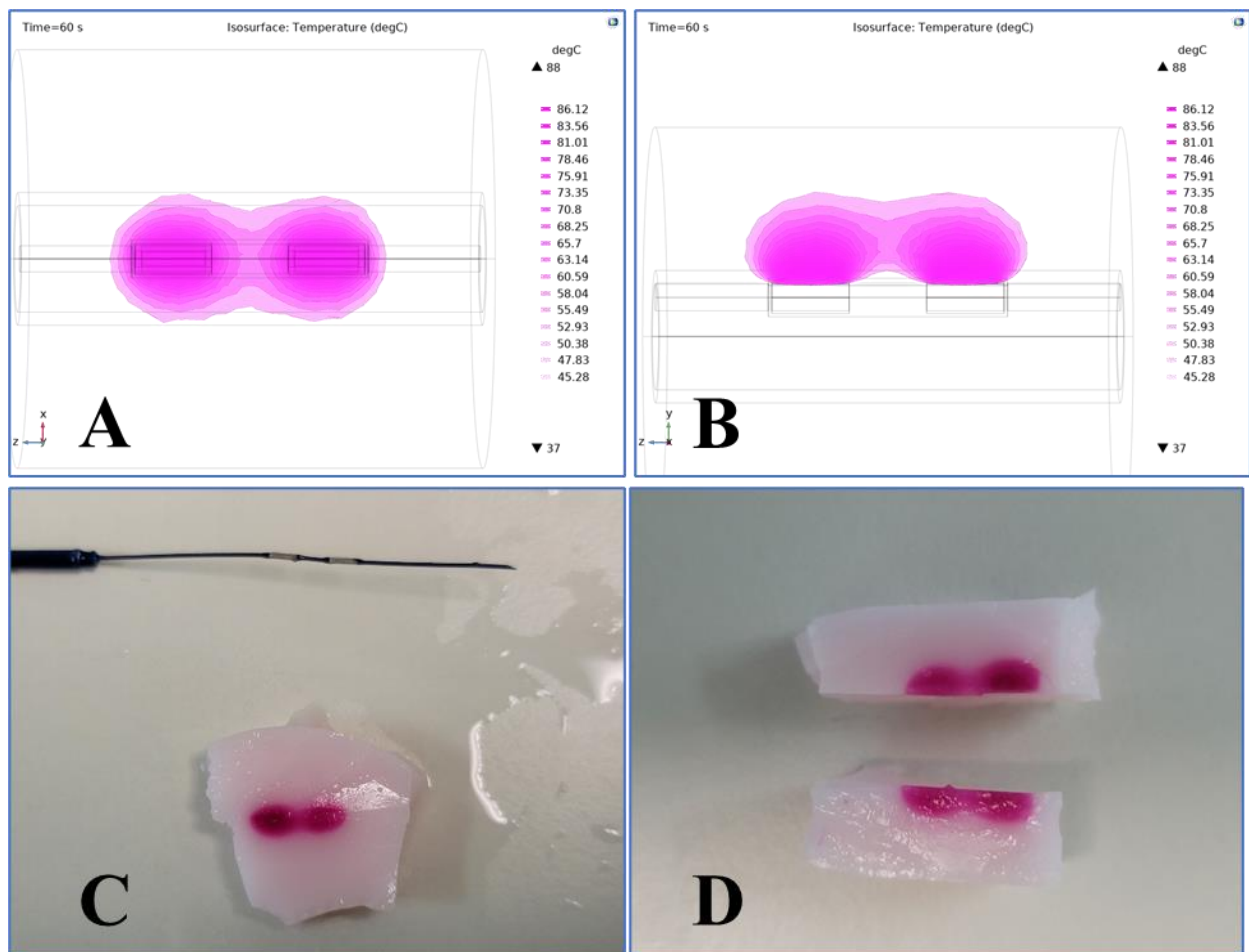


Figure 3.5 Side by side comparison of *in silico* isothermal surfaces and *in vitro* TCP tissue thermal changes. (A) Numerical model prediction of heat distribution from a top view of the electrodes. (B) Same numerical model prediction but in a side view. (C) TCP tissue top view with the ablated zone where electrodes contacted the tissue. (D) TCP tissue sliced to show a side view of ablated tissue penetration depth.

The ablated zone predicted by the model and measured during the *in vitro* experiments with the TCP tissue is summarized in Table 3.2.

Table 3.2 Comparison of ablated zone dimensions between *in silico* and *in vitro* models.

Location	Ablation Zone Dimensions	<i>In Silico</i> (mm)	<i>In Vitro</i> (mm)
Overall	Width (W)	2.1	2
	Length (L)	9.0	9
	Height (H)	1.7	2
Negative Lobe	Width (W)	2.13	2
	Length (L)	3.17	3
Positive Lobe	Width (W)	2.17	2
	Length (L)	3.19	3

There are two noticeable differences where the TCP tissue deviates from the model prediction: 1) the temperature color change in the TCP tissue over the positive electrode shows a higher intensity of color than the tissue over the negative electrode, and 2) the dimensions of the TCP tissue over the positive electrode are more significant than the dimensions of the lobe over the negative electrode. The differences are explained in the numerical model by the Infinite Element Domain (IED) explained in Section 2.2 during the development of the numerical model geometry. The IED is an artificial boundary used to delimit the zone of interest to a small section of the renal artery and limit the extent of the renal system simulated to the target ablation zone. This results in more efficient utilization of computing resources during simulation by eliminating the need to define larger dimensions of surrounding tissues to prevent edge effects from influencing the zone of interest. The IED contrasts with the TCP tissue in the difference in dimensions. IED assumes infinite boundaries, but the TCP tissue was limited by the size that could be produced.

Therefore, the current densities from the positive electrode were also dissipated in the surroundings of the TCP tissue during ablation resulting in a smaller ablation zone than over the negative electrode.

Finally, Figure 3.6 shows the FEM model prediction of blood temperature rises inside the renal artery after completing 60 seconds of RF ablation. Blood temperature inside the artery was maintained at 37°C. A thermal dispersion from the positive electrode over the inside artery wall is noted in the direction of renal blood flow set at 0.7m/s, the density of 1,050 Kg/m³, and normal blood pressure of 120/80 mmHg [29].

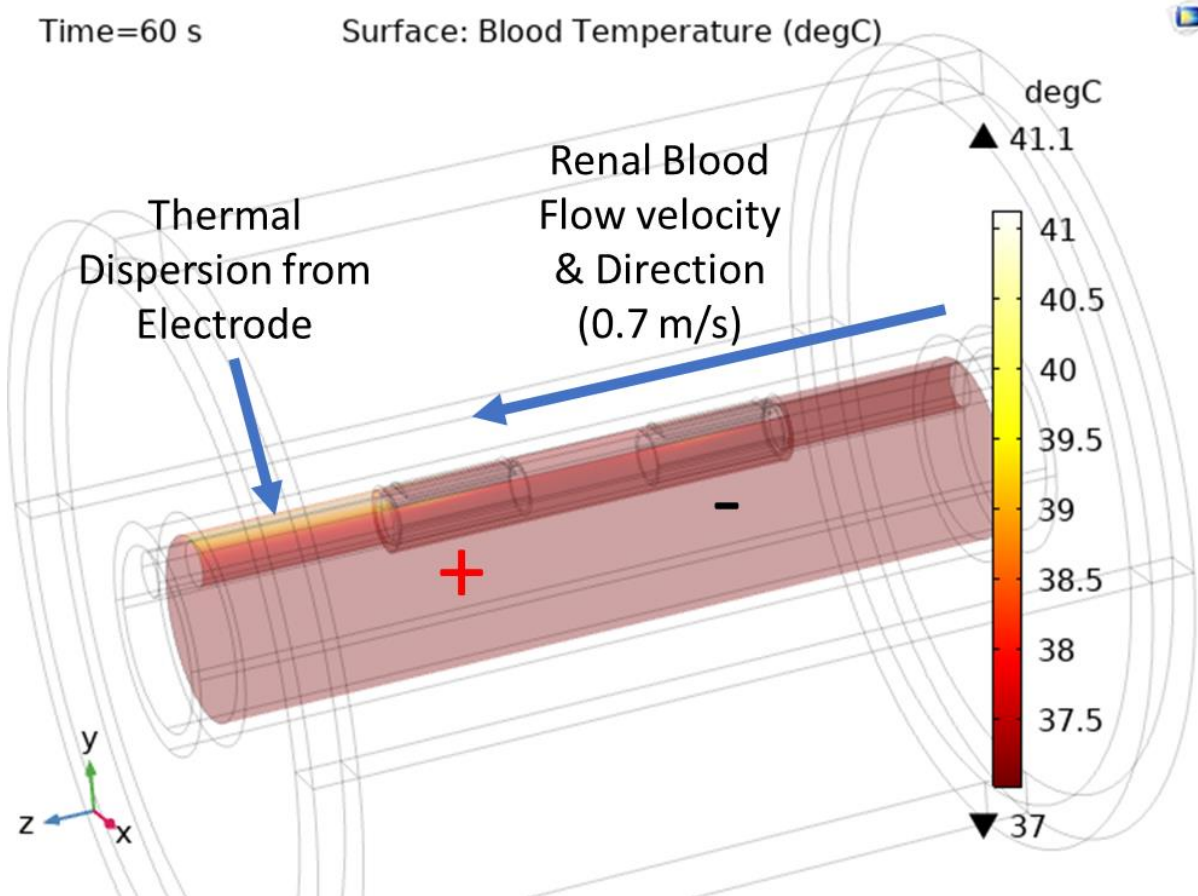


Figure 3.6 FEM model prediction of blood temperature after 60 seconds of RF ablation inside renal artery flowing from the negative to the positive electrode. Blood temperature is predicted to be unaltered from the normal body temperature of 37°C. Thermal dispersion is predicted from the positive electrode and in the direction of the blood flow, which raises the artery wall temperature to 41.1°C.

3.6 Summary

The *in vitro* RF ablation experiments with the bipolar electrodes on the TCP tissue resulted in an efficient and effective alternative for testing the electrode design for RF ablation. Furthermore, compared to *ex vivo* experiments traditionally used, *in vitro* RF ablation of TCP tissue was faster and cost-effective for performing design iterations and optimization.

The TCP tissue experiments validated the FEM numerical model with an excellent correlation between the ablation zone geometry and dimensions predicted *in silico* and measured *in vitro* using TCP tissue. The isothermal surface profile from the computer model in Figure 2.7 predicted an ablation zone with temperatures $\geq 60^{\circ}\text{C}$ after 60 seconds of signal application with a high correlation to the TCP tissue color changes. The model predicted in Figure 2.8 the formation of two elongated lobes over each bipolar electrode, and both lobes were confirmed with the TCP tissue in Figure 3.4. In addition, the model predicted the ablation zone to have dimensions of 2.1 mm (W) x 9.0 mm (L) x 1.7 mm (H) with a positive electrode lobe measuring 2.17 mm (W) x 3.19 mm (L) x 1.7 mm (H) and negative electrode lobe measures 2.13 mm (W) x 3.17 mm (L) x 1.7 mm (H).

The ablated TCP tissue in Figure 2.15 measured 2 mm (W) x 9 mm (L) x 2 mm (H) with both positive and negative electrode lobes measuring approximately 2 mm (W) x 3 mm (L) x 2 mm (H).

Note the close correlation between *in silico* and *in vitro* results, indicating that the computer model accurately predicted the RF ablation zone. Thus, design changes can be performed numerically, saving considerable prototyping time and cost and allowing for time-efficient device optimization. In addition, the application can be extended to other design shapes and ablation targets tissues besides renal artery such as cardiac, tumor, and other therapies.

Chapter 4: *Ex Vivo* Porcine Tissue Experiments

The *In silico* and *in vitro* results demonstrated a close correlation and prediction of the ablated zone on a ThermoChromic phantom (TCP) tissue in Chapters 2 and 3, respectively. In this chapter, the bipolar RF ablation device is tested in a porcine model to validate the previous results. One of the expected issues is that the tissue phantom does not accurately mimic natural porcine tissue. Another issue is the complexity of the renal environment which consists of an artery, connective, and muscle tissue that varies from animal to animal. Once *ex vivo* testing has been completed, the device will be ready for *in vivo* testing in a porcine model.

4.1 Porcine Renal Artery Preparation

Based on the excellent results from *in silico* and *in vitro* testing, the bipolar RF ablation device is at a design and development phase of *ex vivo* tissue evaluation. In addition, numerical design methods have saved multiple build-out iterations compared with the traditional *ex vivo* testing approach since the device was optimized *in silico* and *in vitro* experiments. As a result, the bipolar RF ablation device can be further tested *ex vivo* to investigate and fine-tune the effectiveness of the FEM model parameters and design. More importantly, this is the next step in the proof of concept that, when completed, will allow for *in vivo* porcine model testing before FDA-approved clinical trials.

The *ex vivo* tissue used in this chapter was extracted from a fresh porcine kidney (lot# 2-210324, Animal Technologies, Inc., Texas, USA) still connected to the main aorta. Figure 4.1

shows the received porcine kidneys and main aorta identified by the red arrows with connective tissue between the kidneys and surrounding the arteries.

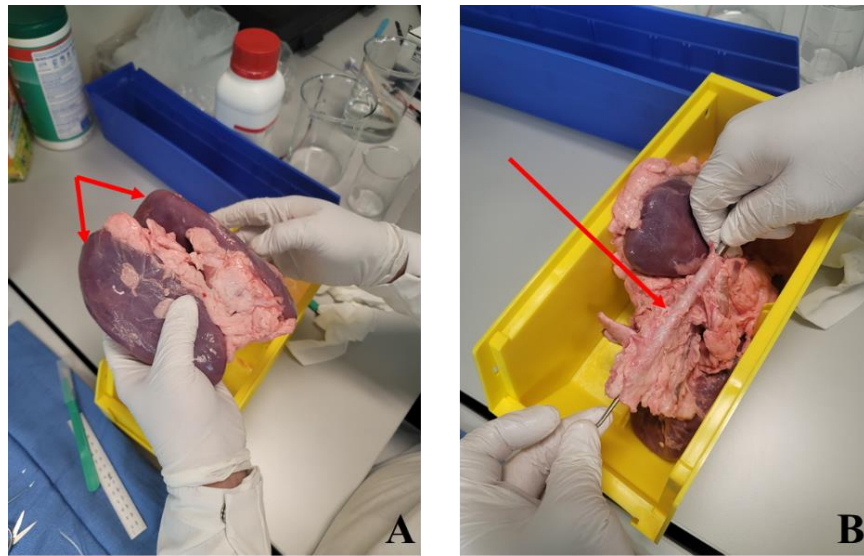


Figure 4.1 *Ex vivo* experimental tissue samples of porcine kidneys. (A) kidneys and (B) identification of the main aorta indicated by the arrows.

The renal artery was identified and dissected from the aorta along with the surrounding connective tissue. The renal artery was split open in half, and an overall tissue block section of a minimum of 20 mm prepared for bipolar RF ablation, as shown in Figure 4.2.

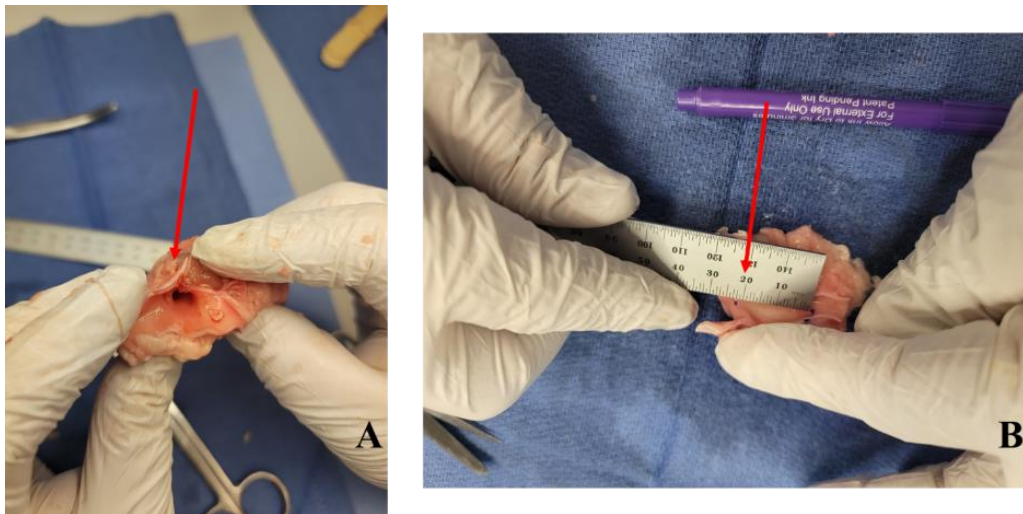


Figure 4.2 *Ex vivo* experimental tissue samples of porcine renal arteries. (A) Porcine renal artery with surrounding tissue dissected (pointed by red arrow). (B) Approximately a section of 20 mm long (pointed by the red arrow) was prepared with renal artery split open for RF ablation.

4.2 Radiofrequency Ablation of Porcine Renal Artery Tissue

4.2.1 First *ex vivo* RF Ablation Experiment

The same RF setup (Figure 3.2) and procedure (Section 3.3 Radiofrequency Ablation of TCP Tissue) was repeated for the *ex vivo* experiment with the dissected section of the porcine renal artery of Figure 4.2 and shown in Figure 4.3. A 500 kHz ablation signal of 3.0 Vp-p was applied using a waveform generator (Agilent, 33220A Santa Clara, CA, USA) and amplified to 60 Vp-p with a fixed-gain linear amplifier (Pendulum, F20A Stockholm, Sweden). An oscilloscope (Tektronix, TDS2001C Beaverton, OR, USA) and a precision multimeter (Fortive, Fluke 8846A Everett, WA, USA) were connected to monitor and confirm that the appropriate ablation signal was applied to the TCP through the electrodes. This setup was maintained and video recorded during each TCP ablation iteration.

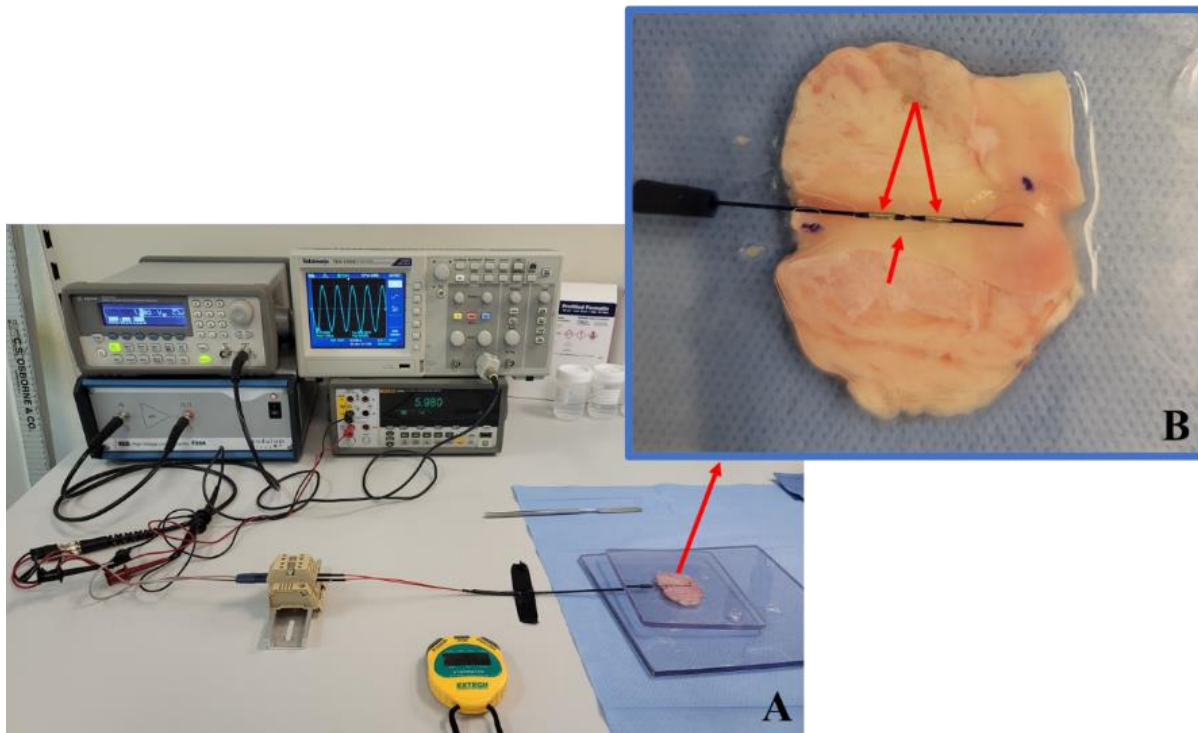


Figure 4.3 *Ex vivo* experiment setup for the ablation porcine renal artery tissue. (A) Equipment setup for RF ablation. (B) Expanded view of porcine renal artery showing bipolar electrodes in the exposed surface and electrical contact with the artery wall. Red arrows indicate bipolar electrodes and porcine renal artery location.

4.2.2 *Ex vivo* Ablated Tissue Storage and Handling

After testing, the porcine *ex vivo* ablated tissue block was immediately transferred to a vial with 10% neutral buffered formalin solution (Azer Scientific, Inc., Morgantown, PA, USA) and labeled for histology evaluation by Dr. Karl Muffly (Director Anatomy Laboratory, Department of Pathology & Cell Biology and Surgery, University of South Florida, FL, USA) as shown in Figure 4.4.

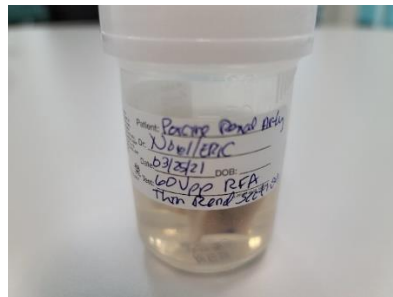


Figure 4.4 Photograph of RF ablated *ex vivo* renal nerve tissue section of Fig. 4.3(b) stored in a 10% neutral buffered formalin solution for histology evaluation. The tissue does not require refrigeration but is maintained at room temperature.

4.2.3 First Histology Results

Histological examination of the RF ablated renal artery section with attached connective tissue was performed. The ablated tissue block was sectioned into 5 nm thick slabs stained with hematoxylin and eosin (H&E). Digital images from H&E-stained histological sections were acquired with a 10X microscope objective lens with a 10X photo objective and 0.6X phototube for a total magnification of 60X.

Figure 4.5 shows two (2) optical micrographs of RF ablated *ex vivo* porcine renal nerve sections after tissue histology. Histological examination did not reveal denaturalized cells; therefore, no ablated tissue was identified in none of the sections.

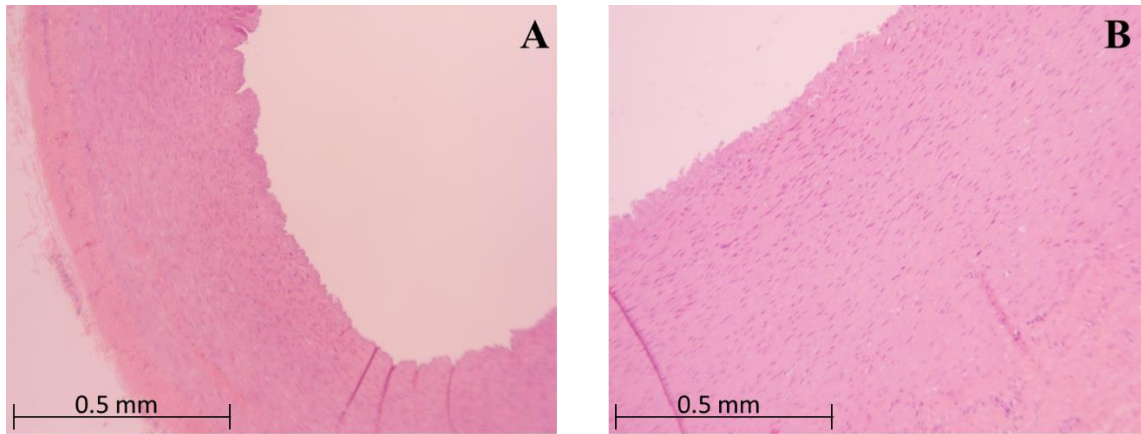


Figure 4.5 Two (2) optical micrographs of RF ablated *ex vivo* renal nerve sections after tissue histology. Denaturalization of cells not observed from this first RFA experiment.

During this first *ex vivo* experiment, a lower current flowing into the electrodes for the same 60 V_{p-p}, 500 kHz excitation signal was noted. This would indicate that the tissue impedance value, based on the TCP tissue phantom simulated, was different from actual porcine tissue. Furthermore, the current was lower than the model/*in vitro* experiment value, indicating a higher tissue impedance. Therefore, the logical next step was to re-visit the model and update the tissue parameters to better predict RF ablation performance *ex vivo*.

4.2.4 Investigation of Porcine Tissue Electrical Characteristics

The disappointing first histology data resulted in a complete revision of the FEM model parameters and the TCP tissue recipe. The electrical properties of the artery wall and connective tissue listed in Table 2.1 were identified as a possible explanation for the difference in the *in vitro* results with *ex vivo* histology of the ablated tissue. Electrical properties, along with their frequency dependence utilized in the model, were obtained from The Foundation for Research on Information Technologies in Society (IT²IS) (Swiss Federal Institute of Technology (ETH) Zurich, Switzerland) and posted on the world wide web page <https://it.is.swiss/virtual-population/tissue-properties/database/dielectric-properties/> [47].

A new batch of fresh *ex vivo* tissue was procured and dissected from fresh porcine kidneys (lot# 2-210526, Animal Technologies, Inc., Texas, USA) to measure the electrical properties (WAMI laboratory, Electrical Engineering Dept. University of South Florida, FL, USA). The *ex vivo* tissue was prepared as two samples: a) preserved in formalin solution and b) maintained pristine and refrigerated for four days. The reasoning was to compare material characteristic differences between preserved and fresh porcine tissue since the timing between the equipment and tissue availability was not immediate. Additionally, new TCP tissue *in vitro* samples was prepared to have a realistic comparison of electrical properties between all tissues studied.

Complex permittivity measurements were performed on the *ex vivo* porcine and TCP tissues with an 85070E Dielectric Probe Kit and an E5063A ENA Series Network Analyzer (Keysight Technologies, Santa Rosa, CA), setup as shown in Figure 4.6.

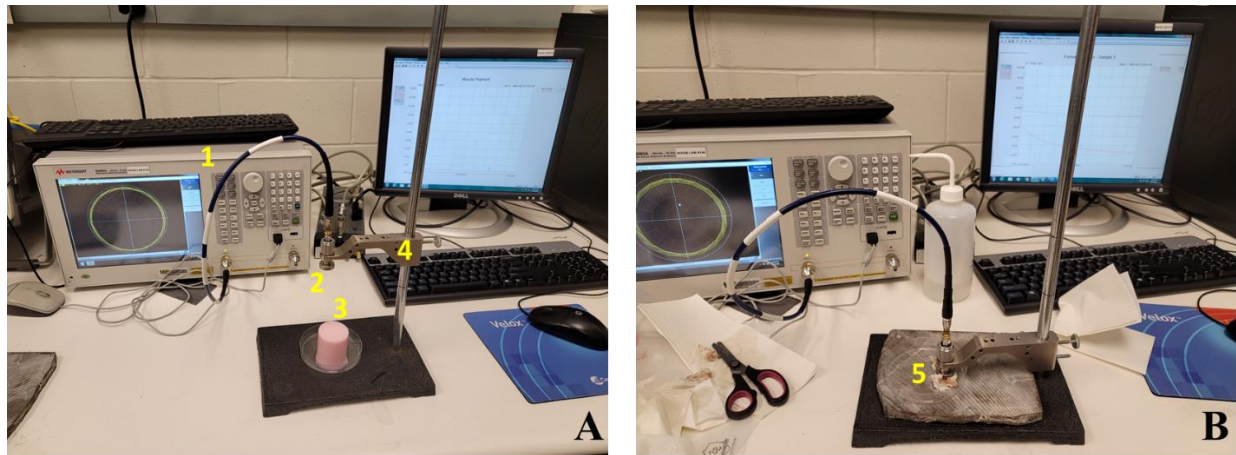


Figure 4.6 Permittivity measurement setup of (A) TCP phantom and (B) *ex vivo* porcine tissue. (1) Network analyzer, (2) Dielectric probe, (3) Thermo-chromic phantom (TCP) tissue, (4) Probe stand, and (5) Porcine *ex vivo* tissue under test.

As per the manufacturer's specification, the available dielectric probe has a frequency range of operation from 200 MHz to 50 GHz. Figure 4.7 and Figure 4.8 illustrate the measured complex impedance components (real and imaginary) versus frequency within the specification range of the dielectric probe (200 MHz to 1 GHz). Since RF ablation is performed at 500 kHz, we

used the complex permittivity values at 200 MHz to investigate conductivity differences between the *ex vivo* and TCP tissues. Calibration trials of the dielectric probe below 200 MHz did not produce reproducible results with any of the tissues; thus, the lowest frequency of valid measurement was 200 MHz. The complex permittivity measurements were performed on three different samples of fresh, preserved, and TCP tissue; then, each tissue type averaged results plotted in Figure 4.7 and Figure 4.8.

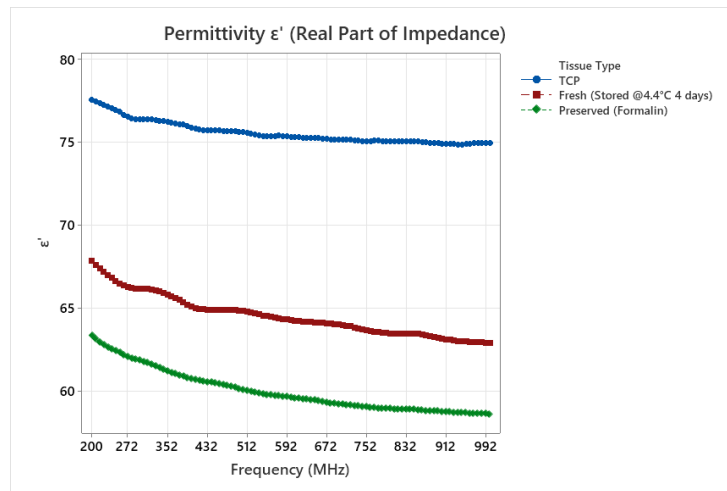


Figure 4.7 Real part (ϵ') of the measured tissue permittivity of fresh porcine tissue (red), preserved porcine tissue (green), and TCP tissue (blue) as a function of frequency (Hz).

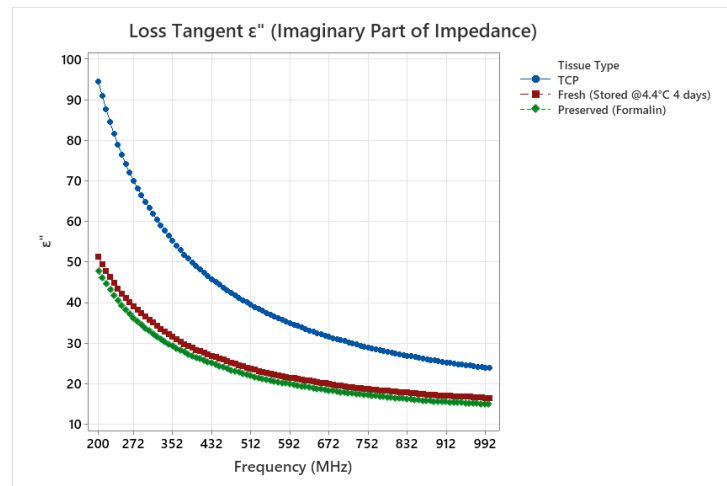


Figure 4.8 Imaginary part (ϵ'') of the measured tissue permittivity of fresh porcine tissue (red), preserved porcine tissue (green), and TCP tissue (blue) as a function of frequency (Hz).

The measured complex permittivity of the three tissues was relatively consistent with the real part of the TCP tissue displaying a higher value while the imaginary part (ϵ'') were very close for both porcine tissues studied. The imaginary part (ϵ''), more commonly described as electric loss tangent ($\tan \frac{\epsilon''}{\epsilon'}$) of the TCP tissue is approximately two orders of magnitude compared to the porcine tissues at 200 MHz.

The average complex permittivity values at 200 MHz for the three different tissues are summarized in Table 4.1. In addition, the porcine tissue was tested both fresh and preserved in formalin to compare the effects of refrigerated tissue, which was stored for four days at 4.4°C. The measurements showed no significant impedance difference between both *ex vivo* tissues.

Table 4.1 Complex Permittivity of TCP and porcine tissues at 200 MHz.

Component	Real Component ϵ_r'	Imaginary Component ϵ_r''
Preserved Tissue	63.3	47.8
Fresh Tissue ^a	67.8	51.3
TCP Tissue	77.2	93.1

^a Tissue was refrigerated for four days at 4.4°C and thawed to room temperature before measurement.

The electrical impedance, Z , is, in general, complex when AC signals are applied to a material and are represented as $Z = \alpha + j\beta$. This is best modeled for tissue as a dielectric medium displaying a complex permittivity behavior $\epsilon^* = \epsilon' - j\epsilon''$. Complex permittivity describes how a material reacts to applied electromagnetic fields, which accounts for the displacement of both free and bound electrons by electric fields ($\mathbf{F} = q\mathbf{E}$) and the orientation of atomic moments by magnetic fields ($\mathbf{F} = q\mathbf{v} \times \mathbf{B}$) [46]. For the materials involved in RF ablation, these responses can be treated as proportional to the applied fields independent of the direction of the field. Therefore, the materials can be assumed to be linear and isotropic to time-varying fields at the specific frequency applied.

The complex permittivity is given by

$$\varepsilon^* = \varepsilon_0 \varepsilon_r = \varepsilon' - j\varepsilon'' \quad (16)$$

where $\varepsilon_0 = \frac{1}{32\pi} \times 10^{-9}$ (F/m), ε_r is the relative permittivity, and ε' is the real and ε'' the imaginary component of the complex permittivity, respectively. The real component ε' is a measure of how much energy from an external field is stored in the material. The imaginary component ε'' is referred to as the loss factor (i.e., loss tangent) and measures how dissipative or lossy a material is to an external field. The loss factor includes the effects of conductivity, resulting in heat loss or Joules heating in the specific case of RF ablation of tissues.

Equation (16) is also expressed in (17), which includes the conductivity of the material [48] and the frequency dependence of the complex permittivity

$$\varepsilon^* = \varepsilon' - j \frac{\sigma}{\omega} \quad (17)$$

$$\varepsilon'' = \frac{\sigma}{\omega} \quad (18)$$

$$\sigma = \omega \varepsilon'' \quad (19)$$

where σ (S/m) is the electrical conductivity of the material and $\omega = 2\pi f$, f (Hz) is the frequency of the applied RF ablation signal. Finally, the complex permittivity components (real and imaginary) measured in Table 4.1 are converted into conductivity σ using equation (19) at a frequency of 200 MHz. The results are summarized in Table 4.2.

Table 4.2 Electrical Parameters of TCP and porcine tissue at 200 MHz.

Component	Complex Permittivity, ε_r^*	Electrical Conductivity, σ (S/m)
Formalin Preserved Porcine Tissue	79.3	0.531
Fresh Porcine Tissue ^a	85.0	0.570
TCP Tissue	123.6	1.061

^a Tissue was refrigerated for four days at 4.4°C and thawed to room temperature before measurement.

Comparing the measured conductivity for both preserved and fresh porcine tissue indicates that the values are close to each other. However, the conductivity of TCP tissue is almost two orders of magnitude greater than the porcine *ex vivo* tissues listed in Table 4.2. These results confirm that the RF signal required for *ex vivo* tissue ablation must be higher for the porcine *ex vivo* than the signal used on the TCP phantom tissue in order to deliver comparable electrical power to the tissues.

Unfortunately, the electrical parameters in Table 4.2 cannot be used to update the FEM model because they are frequency dependent directly, and the dielectric probe could not measure the permittivity below 200 MHz. Therefore, the expeditious alternative to adjust the FEM model and approximate its input parameters to the *ex vivo* tissue experiment is to simply increase the RF signal voltage until tissue ablation is achieved in the model. However, there is a limitation on the maximum voltage that can be applied. In addition, the available fixed-gain linear amplifier Pendulum F20A (Pendulum, Stockholm, Sweden) utilized in the RF ablation setup has a frequency response, as shown in Figure 4.9.

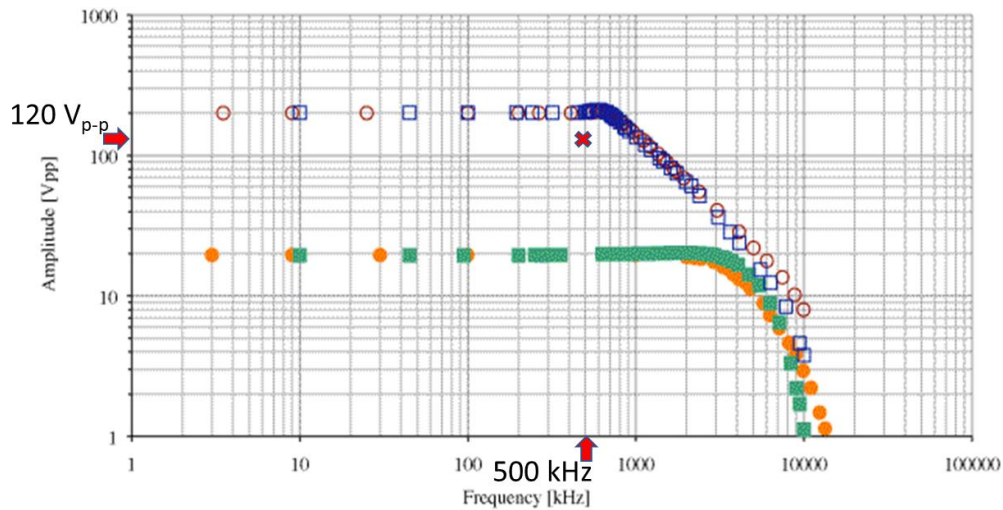


Figure 4.9 Frequency response of the RF linear amplifier Pendulum F20A (Pendulum, Stockholm, Sweden) as a function of load and input voltage. Open circuit (squares blue 200 V, green 20 V)

and a capacitive load of 400 pF (circles red 200V, orange 20 V). The red arrows indicate the new RF ablation voltage of 120 V_{p-p} at 500 kHz.

The maximum peak to peak voltage at 500 kHz, which the linear amplifier can handle without clipping, the output is 120 V_{p-p}, as per Figure 4.9, twice the value used in the FEM model.

Next, the FEM model was updated, and results were compared with another *ex vivo* ablation. Finally, the second RF ablation with an excitation signal of 120 V_{p-p} was performed to examine if tissue ablation was induced and compare it with the adjusted FEM model to complete the investigation and compare results.

4.2.5 Updated FEM Model

Figure 4.10 shows the voltage and current as a function of time during tissue ablation as predicted by the FEM model. Figure 4.10 (A) graphs the current delivered to the ablated tissue during the application of an RF voltage of 60 V_{p-p} (21.21 V_{RMS}). Figure 4.10 (B) graphs the current delivered to the ablated tissue during the application of an RF voltage of 60 V_{p-p} (21.21 V_{RMS}).

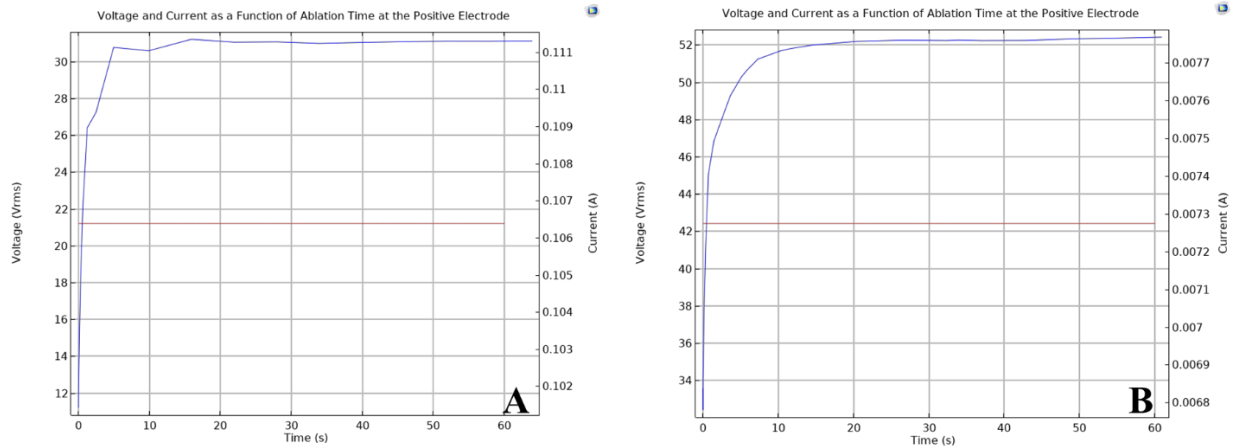


Figure 4.10 RF ablation voltage and current as a function of time. (A) predicted by the FEM model with an RF voltage of 60 V_{p-p} (21.21 V_{RMS}). (B) Adjusted FEM model to an RF voltage of 120 V_{p-p} (42.42 V_{RMS}).

Next, a second *ex vivo* ablation of new porcine tissue will be performed to validate the model based on the voltage and current measured during the *ex vivo* for comparison with the predicted FEM model.

4.2.6 Second *ex vivo* RF Ablation Experiment

A new batch of fresh *ex vivo* tissue was procured and dissected from fresh porcine kidneys (lot# 2-210609, Animal Technologies, Inc., Texas, USA) for RF ablation with the adjusted RF signal level that was calculated from the updated FEM model (i.e., 120 V_{p-p}).

Table 4.3 summarizes the voltage, current, and power delivered by the bipolar RF ablation in the FEM model, the TCP tissue, and the two *ex vivo* tissue experiments. No ablation was identified during the first experiment due to the low power delivered by the applied voltage (caused by the higher tissue impedance). However, to compensate for the lower conductivity of the *ex vivo* tissue, the new adjusted RF ablation voltage applied was 120 V_{p-p} for the second fresh porcine tissue ablation, and the ablated tissue was observed.

Table 4.3 RF Ablation Power Comparison.

RF Ablation Scenario	Voltage ^a (V) (V _{p-p})	Voltage ^b (V) (V _{RMS})	Peak Current (I) (mA)	Peak Power (P) (W) ^c
FEM Model	60	21.21	112	2.38
TCP Tissue	60	21.21	118	2.50
First Fresh Porcine Tissue	60	21.21	4.76	0.10
Second Fresh Porcine Tissue	120	42.42	7.74	0.33

^{a,b} Voltage applied to the tissue

^c Power = V_{RMS} * I

4.2.7 Second Histology Results

Histological examination of the second RF ablated renal artery section tissue block with attached connective tissue was performed. The ablated tissue block was approximately 20 mm. RF ablation was performed with the new signal voltage of 120 V_{p-p}. After ablation, the tissue was immediately transferred to a vial with 10% neutral buffered formalin solution (Azer Scientific, Inc., Morgantown, PA, USA) and labeled for histology evaluation by Dr. Karl Muffly (Director

Anatomy Laboratory, Department of Pathology & Cell Biology and Surgery, University of South Florida, FL, USA). The ablated tissue block was again cut into 5 mm thick slices and stained with hematoxylin and eosin (H&E). Digital images from the H&E-stained histological sections were acquired using a 10X microscope objective with a 10X photo objective and 0.6X phototube for a total magnification of 60X.

The H&E histological sections were strategically dissected to quantify the ablation zone over the positive electrode. Figure 4.10 identifies the sections dissected in relation to the location of the positive electrode. Sample S#1 is the tissue over the center of the positive electrode. Samples S#2 and S#3 were taken 1.5 mm away from S#1 to cover the opposite ends of the positive electrode.

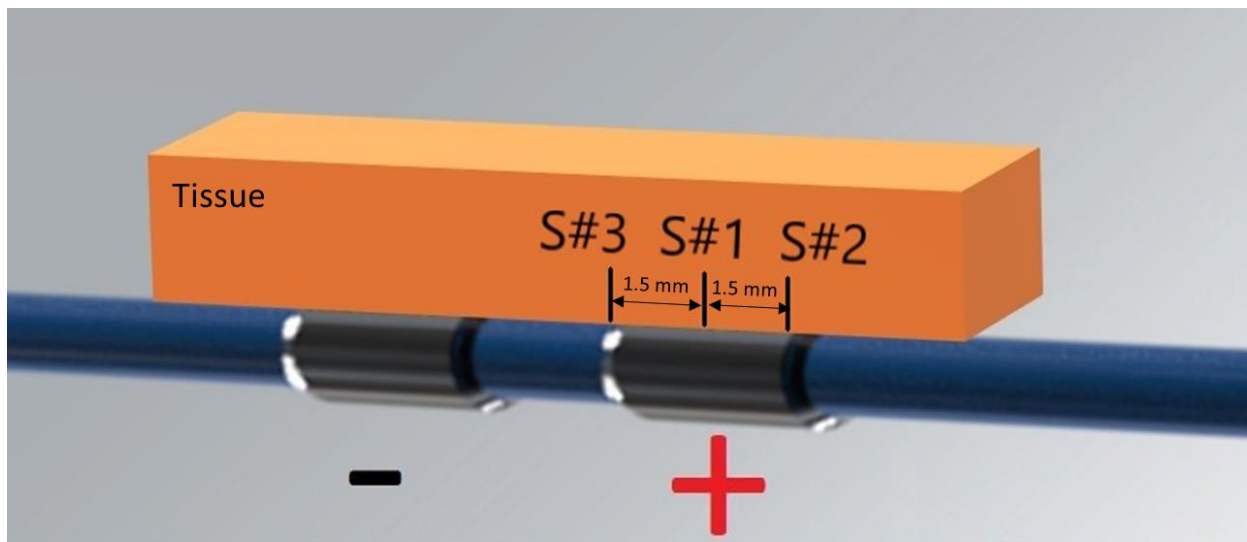


Figure 4.11 H&E histological sections were strategically dissected over the ablated zone. Sample S#1 was taken from the center of the positive electrode, and samples S#2 and S#3 at the electrode edge 1.5 mm from the center of the electrode.

Histological examination revealed denaturalization of cells (ablation) on the endothelium and part of the intima and media areas in the porcine renal artery. Sample S#1, S#2, and S#3 H&E-stained sections are shown in Figure 4.11.

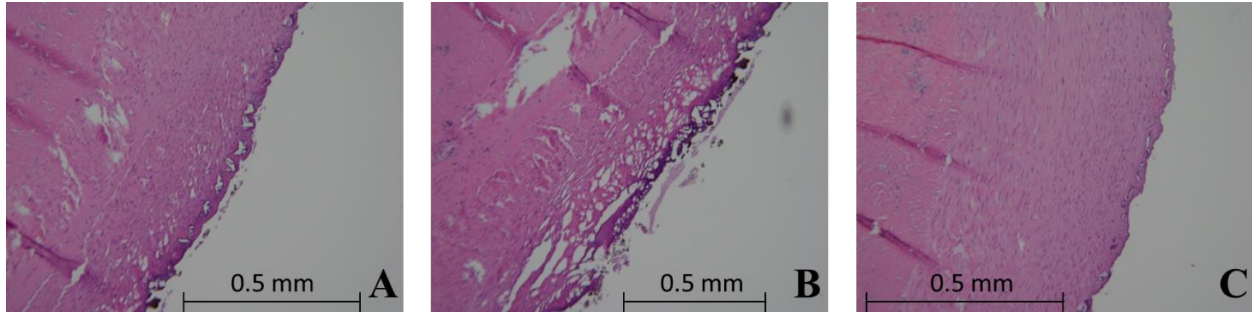


Figure 4.12 Second *ex vivo* tissue ablation experiment H&E-stained sections took over the positive electrode. (A) Sample S#3 from the border closest to the negative electrode, (B) Sample S#1 from the center of the positive electrode, (C) Sample S#2 from the border away from the negative electrode. Histology shows denaturalization of cells in the endothelium and parts of the intima and media S#1.

Histological examination of H&E-stained sections of control samples S#4, S#5, and S#6 confirms no denaturalization of cells, as shown in Figure 4.12.

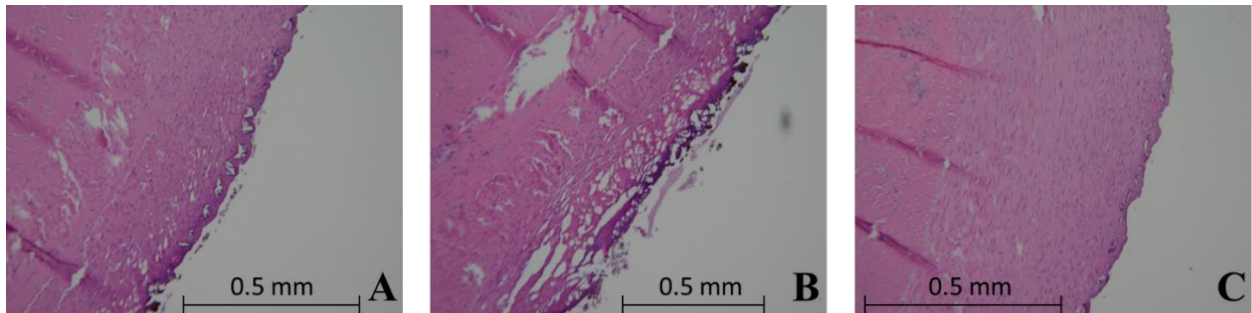


Figure 4.13 Control histology H&E-stained sections of the second *ex vivo* tissue ablation taken from an inactive positive electrode. (A) Sample S#3 from the border closest (proximal) to the negative electrode, (B) Sample S#4 from the center of the positive electrode, (C) Sample S#5 from the border away (distal) of the negative electrode. Histology shows no denaturalization of cells in the control tissue, as expected.

4.3 Comparison Between *In Silico*, *In Vitro* and *Ex Vivo* Results

With the successful ablation of the renal artery *ex vivo*, a dimensional comparison of the ablated zone is summarized in Table 4.4 for the experiments performed *in silico*, *in vitro*, and *ex vivo*. The histology examination focused on the tissue over the positive electrode to maximize available resources since close symmetry between both bipolar electrodes has been predicted in the FEM model and *in vitro* experiment results. Additionally, the *ex vivo* samples S#2 and S#3,

taken at 1.5 mm from the center of the positive electrode, serves as the boundary to define the length of the ablation zone.

Table 4.4 Comparison of ablation zone^a between *in silico*, *in vitro*, and *ex vivo* experiments.

Location	Ablation Zone Dimensions	<i>In Silico</i> (mm)	<i>In Vitro</i> (mm)	<i>Ex vivo</i> (mm)
Positive Electrode	Width (W)	2.17	2	< 0.5

^a Taken over positive electrode

4.4 Summary

Successful *ex vivo* RF ablation was achieved with the bipolar electrode design after adjusting the electrical impedance of porcine tissue with respect to the model (*in silico*) and the RF ablation voltage to the porcine tissue (*ex vivo*). As expected, phantom tissues do not accurately mimic the electrical characteristics of real *ex vivo* porcine tissue due to the complexity of the renal environment, which consists of the artery, connective, muscle tissue, and blood vessels that vary from animal to animal. Therefore, to allow for systematic adjustment in the RF ablation electrical signal applied to the bipolar electrodes, a dielectric probe measurement was conducted in the WAMI lab at USF to measure the impedance of the porcine *ex vivo* tissue block. Analysis of these results, whereby the permittivity and conductivity of the tissue were used to update the *in silico* model, resulted in a successful ablation as confirmed by histology analysis. The most important outcome of this result is the high confidence level that we now have with the computer model in predicting RF ablation in porcine tissue.

At this point, the final research aim of this dissertation has been completed, and further development, along with some exciting ideas to best prepare this technology for commercial use, will be presented in the next and final chapter of this dissertation.

Chapter 5: Conclusion and Future Work

5.1 Summary

5.1.1 *In Silico*, *In Vitro* and *Ex Vivo* RF Ablation Analysis and Comparisons

The isothermal plot from the computer model in Figure 2.7 predicted that the tissue volume reached a temperature of $\geq 60^{\circ}\text{C}$ after an RF ablation signal exposure of 60 seconds due to induced Joule heating. The ablated area consisted of two elongated lobes with an approximate maximum dimension of 4 mm x 10 mm x 4 mm (length x width x height).

The ablated ThermoChromic Phantom (TCP) *in vitro* tissue was measured and compared with the isothermal plot from the computer model *in silico* and shown in Figure 3.5. Note the excellent correlation between simulated *in silico* and experimental *in vitro* defined ablated zones (4 x 10 x 4 mm vs. 3 x 8.5 x 3.5 mm), indicating that the computer model accurately predicted the Radiofrequency (RF) ablation zone geometry *in vitro*. Next, two *ex vivo* experiments with the porcine renal artery were performed to validate the Finite Element Model (FEM) and confirm the *in vitro* TCP tissue results. The first *ex vivo* ablation experiment used the predicted ablation voltage level of 60 V_{P-P} needed to achieve a tissue temperature of $\geq 60^{\circ}\text{C}$, and it was observed that significantly less current flowed compared to the *in vitro* experiment. That is to say, the delivered power was much lower, which could be an indication of higher tissue impedance from the porcine tissue block with respect to the TCP phantom.

Furthermore, tissue histology confirmed that no ablation had occurred under these conditions. Next, using a dielectric measurement probe in the WAMI laboratory (Dept. of

Electrical Engineering, USF, FL), tissue permittivity was measured. Indeed, the TCP tissue displayed an electrical conductivity approximately two orders of magnitude greater than the porcine tissue block. The required RF ablation parameters were then adjusted, both in the model and subsequent experimentation, and a second *ex vivo* experiment was performed with the new input power (voltage 120 V_{P-P}) values. Histology performed post-ablation showed an excellent correlation between the TCP tissue (*in vitro* experiment) and *ex vivo* porcine tissue ablation experiments. Consequently, the updated *in silico* model is now believed to be correct and can be used for further design and development iterations without the need for costly hardware build-out and testing in animal tissue, which is also very costly and time-consuming.

5.2 Discussion

The use of renal denervation devices to alter a patient's nervous system in the vicinity of the renal artery has been demonstrated to reduce critical patient blood pressure when pharmacological solutions are not viable [32]. However, to date, a practical, clinically consistent RF ablation catheter, which is under intense development worldwide, has not entered the marketplace in the USA due to a lack of FDA approval. Therefore, this research aimed to begin developing an effective RF ablation device that uses low power, does not inhibit blood flow during treatment, and does not require the use of a patient grounding pad while being capable of effectively targeting renal nerves for denervation.

While several RF ablation catheter devices with the CE mark, as listed in Table 1.1, are authorized for use in the European Union (EU), all are single electrode devices with the need of a grounding or indifferent pad which is fixed on the skin of the patient and requiring high power ablation generators (typically from 50 to 100 W RF generators are used) which risks patient skin burns. At the time of this investigation, the only bipolar renal denervation device with a CE mark

is the Vessix™ (Boston Scientific, Marlborough, MA), which incorporates a balloon catheter with multiple electrodes. This has the disadvantage that once inflated; the balloon blocks renal blood flow during ablation.

This research produced a bipolar basket catheter design that does not require a balloon, so it has the advantage of not blocking renal blood flow during ablation. Furthermore, there is no need for cooling since the catheter has short ablation times and lower required power than existing designs to perform the ablation. RF ablation devices have evolved from single unipolar electrodes (the original Symplicity HT1™, Medtronic, Santa Clara, CA, USA) to multi-electrode unipolar systems (Spyral™) [28] but still requiring grounding pads.

This investigation focused on the bipolar electrode for RF ablation with the electrode design, dimensions, geometry, and ablation area simulated and optimized via FEM *in silico*. The simulation included the surrounding artery and connective tissue's electrical properties to predict the ablation zone dimensions to achieve renal nerve ablation. In addition, a ThermoChromic Phantom (TCP) tissue was used to compare the *in vitro* ablation zone with simulations. While the TCP starts changing color at 60°C, there is considerable variability to determine the exact location where the TCP starts to display a temperature color transition. Nevertheless, the TCP allows visual and quantitative comparison of the geometry, shape, and form of the ablation zone, closely matching the computational simulation. Therefore, the developed FEM can further optimize the catheter design for accurate renal nerve ablation in animal models *in vivo* to pave the way for clinical validation.

Further experiments were performed *ex vivo* to determine how well the *in silico* and *in vitro* data translates to actual porcine tissue. As expected, actual porcine tissue displays different electrical characteristics compared with the tissue phantom and literature values. Two (2) *ex vivo*

ablation experiments were conducted: The first used the *in silico* FEM predicted voltage value of 60 V_{P-P} and resulted in a null result (no ablation). It was observed that the current flow during ablation was significantly lower than measured *in vitro*, indicating that the porcine tissue block had significantly higher electrical impedance than the phantom tissue block. Dielectric constant (complex permittivity) measurements were then made using a vector network analyzer and dielectric probe from 200 MHz to 1 GHz. These measurements confirmed the higher electrical impedance of the *ex vivo* porcine tissue block. The change in permittivity measured was used to calculate the porcine tissue's electrical conductivity. It was found to be approximately two orders of magnitude lower, thus validating the observation that lower current was caused by higher tissue impedance. The numerical model was then updated, and the predicted RF voltage needed to confirm ablation, as observed *in vitro*, was found to be ~120V_{P-P}. A second *ex vivo* experiment with the new RF signal voltage value and ablation was observed via tissue histology. This marked the successful experimental completion of this doctoral dissertation.

This updated computational RF ablation model can now be used to estimate ablation zones in the renal artery for renal denervation (RD) in patients with hypertension. The model provides an efficient iterative platform to design and refine RF ablation electrodes for targeted ablation geometries and dimensions. In addition, the model can be extended to other anatomical landmarks to predict the RF ablation pattern in the targeted zone. The TCP phantom complements this model to provide a relatively simple and cost-effective *in vitro* medium for quick feedback to the computational model from RF ablation experiments, allowing short iteration times during catheter development compared to traditional, costly, and time-consuming animal and human trials.

5.3 Conclusion

The results from this work have demonstrated the feasibility of implementing the bipolar RF ablation device and deserve further study and development as a potential RD device. The bipolar configuration and innovative electrode design ensure that the current density is focused on the target tissue, reducing the energy transferred to renal blood and thus reducing the need for cooling. Furthermore, the electrode exposure window can be modified in shape and dimensions based on the intended location and geometry desired for ablation. This model and TCP tissue can be used to investigate other ablation applications, e.g., tumor ablation, to design an electrode for the specifically intended zone. Further *ex vivo* and *in vivo* studies are warranted to further validate this new bipolar catheter system.

5.4 Future Work

Further characterization of the electrical parameters at the RF ablation frequency in *ex vivo* porcine tissue is needed to fine-tune the FEM model with natural tissue further. Understanding the limitations between TCP tissue and *ex vivo* tissue reinforced the need for additional electrical characterization of natural tissue. Nevertheless, a new formulation of the TCP with closer values to the tissue electrical impedance measurements will increase the benefits of *in vitro* testing with TCP tissue which became evident during this investigation by the intensive iterations between the *silicon* model and TCP tissue ablations. The FEM model and TCP provided an efficient combination to iterate design changes instead of costly and time-consuming *ex vivo* experimentation. After that iteration process, the design of the bipolar electrodes was at a more robust design level and ready for *ex vivo* experiments.

The impedance differences in the porcine tissue triggered the idea of developing an RF generator with the capability of dynamic impedance matching (DIM). This functionality will

incorporate electronics to measure reflected power from the tissue due to the impedance mismatch with the generator and dynamically adjust the capacitance to maintain maximum power transfer to the tissue during ablation. This will not only result in a more efficient energy transfer to the ablation zone (decreasing power requirements to increase patient comfort and safety) but will allow for more repeatable clinical trials once this RF ablation catheter reaches this stage of development.

After further confirming tissue electrical parameters, the bipolar RF ablation catheter should be tested in an *in vivo* setup. The animal's blood pressure can be monitored before and after ablation to quantify the immediate effects of the renal ablation. In addition, blood pressure follow-up measurements can determine the duration of the renal ablation effects on blood pressure.

The bipolar RF ablation device assembled in a 6 Fr provides the flexibility for adding multiple features to improve the surgeons' experience. For example, a flushing center lumen can inject a standard saline solution to prepare renal artery surface to receive the electrodes and improve electrical contact. Additionally, the basket catheter design provides additional electrodes, increasing freedom in shaping the RF ablation zone(s).

The basket catheter design with multiple PtIr electrodes provides the basis for potential future investigation of renal nerve electrical signal mapping. This potential functionality added to the existing RF ablation capability will result in a single-use device integrating mapping and ablation capability during one surgical procedure. Follow-up on research may investigate the capability of the bipolar electrodes in contact with tissue near the renal artery to detect and measure renal nerve activity. The mapping process should detect the circumferential nerve location (or locations) with the highest burst of action potentials and switch to ablation mode with the same electrodes that measured the signals, thus improving ablation accuracy.

References

- [1] Mancia, Giuseppe, et al. Manual of Hypertension of the European Society of Hypertension. Third edition., CRC Press, Taylor & Francis Group, 2019.
- [2] High Blood Pressure Fact Sheet|Data & Statistics|DHDS|CDC. 9 Jan. 2019, https://www.cdc.gov/dhds/data_statistics/fact_sheets/fs_bloodpressure.htm.
- [3] “Diagnosing and Treating Resistant Hypertension.” American Heart Association, 13 Oct. 2019, <https://newsroom.heart.org/news/diagnosing-and-treating-resistant-hypertension>.
- [4] Carey, Robert M., et al. “Resistant Hypertension American Heart Association.” Hypertension, vol. 72, no. 5, Nov. 2018. DOI.org (Crossref), doi:10.1161/HYP.0000000000000084.
- [5] Wilhelm, Patricia Brady, et al. Human Anatomy and Physiology : Based on Schaum’s Outline of Theory and Problems of Human Anatomy and Physiology. McGraw-Hill Professional, 2001. EBSCOhost, search.ebscohost.com/login.aspx?direct=true&db=nlebk&AN=66532&site=eds-live.
- [6] Froeschl, Michael, et al. “Renal Sympathetic Denervation for Resistant Hypertension.” Canadian Journal of Cardiology, vol. 29, no. 5, May 2013, pp. 636–38. ScienceDirect, doi:10.1016/j.cjca.2013.02.019.

- [7] Tortora, Gerard J., and Bryan Derrickson. Principles of Anatomy & Physiology, 14th edition., Wiley, 2014. EBSCOhost, search.ebscohost.com/login.aspx?direct=true&db=cat00847a&AN=usflc.032933332&site=eds-live.
- [8] Sata, Yusuke, et al. “Role of the Sympathetic Nervous System and Its Modulation in Renal Hypertension.” *Frontiers in Medicine*, vol. 5, Mar. 2018. PubMed Central, doi:10.3389/fmed.2018.00082.
- [9] Schlaich, Markus P., Henry Krum, Paul A. Sobotka, and Murray D. Esler. “Renal Denervation and Hypertension.” *American Journal of Hypertension* 24, no. 6 (June 1, 2011): 635–42. <https://doi.org/10.1038/ajh.2011.35>.
- [10] How does oxidative stress affect the body?. *Medical News Today, Newsletter, Medically reviewed by Stacy Sampson, D.O. — Written by Jamie Eske on April 3, 2019*, <https://www.medicalnewstoday.com/articles/324863>.
- [11] Sakakura, Kenichi, et al. “Anatomic Assessment of Sympathetic Peri-Arterial Renal Nerves in Man.” *Journal of the American College of Cardiology*, vol. 64, no. 7, Aug. 2014, pp. 635–43. ScienceDirect, doi:10.1016/j.jacc.2014.03.059.
- [12] Bradford, J. Rose. “The Innervation of the Renal Blood-Vessels.” *Proceedings of the Royal Society of London*, vol. 45, 1888, pp. 362–68. JSTOR.
- [13] Author unknown. Neurosurgical treatment, indications and results (chapter 7, methods of operation). *J Intern Med*. 1947;127:72–76.
- [14] Adson AW, McCraig W, Brown GE. Surgery in its relation to hypertension. *Surg Gynecol Obstet*. 1936;62:314–331.

- [15] Weiss E. Recent advances in the pathogenesis and treatment of hypertension, a review. *Psychosom Med.* 1939;1:180–198.
- [16] Sen SK. Some observations on decapsulation and denervation of the kidney. *Brit J Urol.* 1936;8:319–328.
- [17] Page IH, Heuer GJ. The effect of renal denervation on the level of arterial blood pressure and renal function in essential hypertension. *J Clin Invest.* 1935;14:27–30.
- [18] Page IH, Heuer GJ. The effect of renal denervation on patients suffering from nephritis. *J Clin Invest.* 1935;14:443–458.
- [19] Peet MM. Hypertension and its surgical treatment by supradiaphragmatic splanchnicectomy. *Am J Surg.* 1948;LXXV:48–68.
- [20] Papademetriou Vasilios, et al. “Renal Nerve Ablation for Resistant Hypertension.” *Circulation*, vol. 129, no. 13, Apr. 2014, pp. 1440–51,4-5. www-ahajournals-org.ezproxy.lib.usf.edu (Atypon), doi:10.1161/CIRCULATIONAHA.113.005405.
- [21] Smithwick RH, Thompson JE. Splanchnicectomy for essential hypertension; results in 1,266 cases. *J Am Med Assoc.* 1953;152:1501–1504.
- [22] Peet MM, Woods WW, Braden S. The surgical treatment of hypertension. *JAMA.* 1940;115:1875–1885.
- [23] Greene, Jeremy A. “Releasing the Flood Waters: Diuril and the Reshaping of Hypertension.” *Bulletin of the History of Medicine*, vol. 79, no. 4, 2005, pp. 749–94. Project MUSE, doi:10.1353/bhm.2005.0153.
- [24] Freis ED, Wanko A, Wilson IM, Parrish AE. Treatment of essential hypertension with chlorothiazide (diuril); its use alone and combined with other antihypertensive agents. *J Am Med Assoc.* 1958;166:137–140.

- [25] Webb RL, Brody MJ. Functional identification of the central projections of afferent renal nerves. *Clin Exp Hypertens A*. 1987;9(suppl 1):47–57.
- [26] Campese VM, Kogosov E. Renal afferent denervation prevents hypertension in rats with chronic renal failure. *Hypertension*. 1995;25(4 pt 2):878–882.
- [27] Converse RL Jr, Jacobsen TN, Toto RD, Jost CM, Cosentino F, Fouad-Tarazi F, Victor RG. Sympathetic overactivity in patients with chronic renal failure. *N Engl J Med*. 1992;327:1912–1918.
- [28] Sata, Yusuke, et al. “Role of the Sympathetic Nervous System and Its Modulation in Renal Hypertension.” *Frontiers in Medicine*, vol. 5, Mar. 2018. PubMed Central, doi:10.3389/fmed.2018.00082.
- [29] Greene, Ernest R., et al. “Noninvasive Characterization of Renal Artery Blood Flow.” *Kidney International*, vol. 20, no. 4, Oct. 1981, pp. 523–29. DOI.org (Crossref), doi:10.1038/ki.1981.171.
- [30] Kapil, Vikas, et al. “Renal Sympathetic Denervation – A Review of Applications in Current Practice.” *Interventional Cardiology Review*, vol. 9, no. 1, Mar. 2014, pp. 54–61. PubMed Central, doi:10.15420/icr.2011.9.1.54.
- [31] Patel, Hitesh C., et al. “Renal Denervation for the Management of Resistant Hypertension.” *Integrated Blood Pressure Control*, Dove Medical Press, 3 Dec. 2015, doi:10.2147/IBPC.S65632.
- [32] Patel, Hitesh C., et al. “Renal Denervation for the Management of Resistant Hypertension.” *Integrated Blood Pressure Control*, 3 Dec. 2015, doi:10.2147/IBPC.S65

- [33] COMSOL Multiphysics® v. 5.6. www.comsol.com. COMSOL AB, Stockholm, Sweden.
- [34] Sakakura, Kenichi, et al. “Anatomic Assessment of Sympathetic Peri-Arterial Renal Nerves in Man.” *Journal of the American College of Cardiology*, vol. 64, no. 7, Aug. 2014, pp. 635–43. DOI.org (Crossref), doi:10.1016/j.jacc.2014.03.059.
- [35] Leertouwer, Trude C., et al. “In-Vitro Validation, with Histology, of Intravascular Ultrasound in Renal Arteries.” *Journal of Hypertension*, vol. 17, no. 2, Feb. 1999, pp. 271–77.
- [36] Perez, Noel. “ABLATION CATHETERS AND SYSTEMS.” US Patent Application 63/082,398. 23 September 2020.
- [37] Lee, Bruce B., and Steve P. Yu. “Radiofrequency Ablation of Uterine Fibroids: A Review.” *Current Obstetrics and Gynecology Reports*, vol. 5, no. 4, Dec. 2016, pp. 318–24. DOI.org (Crossref), doi:10.1007/s13669-016-0183-x.
- [38] Haemmerich, Dieter, and David J. Schutt. “RF Ablation at Low Frequencies for Targeted Tumor Heating: In Vitro and Computational Modeling Results.” *IEEE Transactions on Biomedical Engineering*, vol. 58, no. 2, Feb. 2011, pp. 404–10. IEEE Xplore, doi:10.1109/TBME.2010.2085081.
- [39] Tungjitkusolmun, S., et al. “Three-Dimensional Finite-Element Analyses for Radio-Frequency Hepatic Tumor Ablation.” *IEEE Transactions on Biomedical Engineering*, vol. 49, no. 1, Jan. 2002, pp. 3–9. IEEE Xplore, doi:10.1109/10.972834.

- [40] Rossmann, Christian, and Dieter Haemmerich. "Review of Temperature Dependence of Thermal Properties, Dielectric Properties, and Perfusion of Biological Tissues at Hyperthermic and Ablation Temperatures." *Critical Reviews in Biomedical Engineering*, vol. 42, no. 6, 2014, pp. 467–92. PubMed Central, doi:PMID: 25955712 PMCID: PMC4859435.
- [41] Zurbuchen, Urte, et al. "Determination of the Temperature-Dependent Electric Conductivity of Liver Tissue Ex Vivo and in Vivo: Importance for Therapy Planning for the Radiofrequency Ablation of Liver Tumours." *International Journal of Hyperthermia*, vol. 26, no. 1, Jan. 2010, pp. 26–33. DOI.org (Crossref), doi:10.3109/02656730903436442.
- [42] Berjano, Enrique J. "Theoretical Modeling for Radiofrequency Ablation: State-of-the-Art and Challenges for the Future." *BioMedical Engineering OnLine*, vol. 5, no. 1, 2006, p. 24. DOI.org (Crossref), doi:[10.1186/1475-925X-5-24](https://doi.org/10.1186/1475-925X-5-24).
- [43] Iserson, Kenneth V. "J.-F.-B. Charrière: The Man behind the 'French' Gauge." *The Journal of Emergency Medicine*, vol. 5, no. 6, Nov. 1987, pp. 545–48. ScienceDirect, doi:10.1016/0736-4679(87)90218-6.
- [44] Mikhail, Andrew S., et al. "Evaluation of a Tissue-Mimicking Thermochromic Phantom for Radiofrequency Ablation." *Medical Physics*, vol. 43, no. 7, July 2016, pp. 4304–11. PubMed Central, doi:10.1118/1.4953394.
- [45] Townsend, Raymond R., et al. "Catheter-Based Renal Denervation in Patients with Uncontrolled Hypertension in the Absence of Antihypertensive Medications (SPYRAL HTN-OFF MED): A Randomised, Sham-Controlled, Proof-of-Concept Trial." *The Lancet*, vol. 390, no. 10108, Nov. 2017, pp. 2160–70. ScienceDirect, doi:10.1016/S0140-6736(17)32281-X.

- [46] Ramo, Simon, et al. Fields and Waves in Communication Electronics. J. Wiley, 1965.
- [47] Dielectric Properties » IT'IS Foundation. 4 Apr. 2020, <https://itis.swiss/virtual-population/tissue-properties/database/dielectric-properties/>.
- [48] Chen, Wai-Kai. (2005). Electrical Engineering Handbook. Elsevier. Retrieved from <https://app.knovel.com/hotlink/toc/id:kpEEH00005/electrical-engineering/electrical-engineering>

Appendix A: Copyright Permissions

The permission below is for the use of Figure 1.2.

ELSEVIER LICENSE TERMS AND CONDITIONS

Apr 05, 2021

This Agreement between Noel Perez ("You") and Elsevier ("Elsevier") consists of your license details and the terms and conditions provided by Elsevier and Copyright Clearance Center.

License Number	5042140896711
License date	Apr 04, 2021
Licensed Content Publisher	Elsevier
Licensed Content Publication	Canadian Journal of Cardiology
Licensed Content Title	Renal Sympathetic Denervation for Resistant Hypertension
Licensed Content Author	Michael Froeschl,Adnan Hadziomerovic,Marcel Ruzicka
Licensed Content Date	May 1, 2013
Licensed Content Volume	29
Licensed Content Issue	5
Licensed Content Pages	3
Start Page	636
End Page	638
Type of Use	reuse in a thesis/dissertation
Portion	figures/tables/illustrations
Number of figures/tables/illustrations	1
Format	both print and electronic
Are you the author of this Elsevier article?	No
Will you be translating?	No
Title	In Silico, In Vitro and Ex Vivo Development of a New Bipolar Radiofrequency Ablation Device for Renal Denervation
Institution name	University of South Florida
Expected presentation date	Jun 2021
Order reference number	Figure 1.1 of Thesis
Portions	Figure 1. Functional anatomy of renal sympathetic innervation.
Requestor Location	Noel Perez 
	Attn: Noel Perez
Publisher Tax ID	98-0397604
Total	0.00 USD
Terms and Conditions	

INTRODUCTION

1. The publisher for this copyrighted material is Elsevier. By clicking "accept" in connection with completing this licensing transaction, you agree that the following terms and conditions apply to this transaction (along with the Billing and Payment terms and conditions established by Copyright Clearance Center, Inc. ("CCC"), at the time that you opened your Rightslink account and that are available at any time at <http://myaccount.copyright.com>).

The permission below is for the use of Figure 1.3.

4/8/2021 RightsLink - Your Account

**ELSEVIER LICENSE
TERMS AND CONDITIONS**

Apr 08, 2021

This Agreement between Noel Perez ("You") and Elsevier ("Elsevier") consists of your license details and the terms and conditions provided by Elsevier and Copyright Clearance Center.

License Number	5044540188447
License date	Apr 08, 2021
Licensed Content Publisher	Elsevier
Licensed Content Publication	Journal of the American College of Cardiology
Licensed Content Title	Anatomic Assessment of Sympathetic Peri-Arterial Renal Nerves in Man
Licensed Content Author	Kenichi Sakakura,Elena Ladich,Qi Cheng,Fumiyuki Otsuka,Kazuyuki Yahagi,David R. Fowler,Frank D. Kolodgie,Renu Virmani,Michael Joner
Licensed Content Date	Aug 19, 2014
Licensed Content Volume	64
Licensed Content Issue	7
Licensed Content Pages	9
Start Page	635
End Page	643
Type of Use	reuse in a thesis/dissertation
Portion	figures/tables/illustrations
Number of figures/tables/illustrations	1
Format	both print and electronic
Are you the author of this Elsevier article?	No
Will you be translating?	No
Title	In Silico, In Vitro and Ex Vivo Development of a New Bipolar Radiofrequency Ablation Device for Renal Denervation
Institution name	University of South Florida
Expected presentation date	Jun 2021
Order reference number	Figure 1.3 Physiological diagram
Portions	CENTRAL ILLUSTRATION Proposed Diagram of Renal Artery and Circumferential Peri-Arterial Nerve Location
Requestor Location	Noel Perez 

<https://s100.copyright.com/MyAccount/web/jsp/viewprintablelicensefrommyorders.jsp?ref=b3f52b2b-cac0-4d5c-a95a-c0e7cf90f645&email=> 1/5

The permission below is for the use of Figure 1.5.

nperez21@outlook.com

From: Shannon Ainsworth <shannonainsworth@dovepress.co.uk>
Sent: Wednesday, April 14, 2021 4:47 AM
To: nperez21@outlook.com
Cc: Claire Wilshaw
Subject: ACI211719 - Renal Denervation System/Patel - Permission Granted

Dear Dr. Noel Perez

Thank you for your below enquiry.

I am pleased to confirm that we grant permission to use figure 3 for your thesis and at no cost.

*Renal denervation for the management of resistant hypertension
Patel H et al
Integrated Blood Pressure Control 2015 8 57-69*

Please note:

- The figure must be fully cited
- Dove Medical Press must be acknowledged as the original publisher
- Any other re-use in the future will require separate permission to be requested
- No transfer of copyright should be inferred or implied

Please let me know should you have any further questions and I wish you all the best with your thesis and studies.

Best Regards

Shannon

Shannon Ainsworth
Reprints Team
Dove Medical Press Limited

Beechfield House,
Winterton Way,
Macclesfield SK11 0LP
United Kingdom
www.dovepress.com

Company registration number: 4967656
Registered in England and Wales. Registered address 5 Howick Place, London, SW1P 1WG.
VAT Number: GB 385 4626 36

Dove Medical Press is part of Taylor & Francis Group, the Academic Publishing Division of Informa PLC

T: +44 (0)1625 509134
F: +44 (0)1625 817933

E: shannonainsworth@dovepress.co.uk

The information in this facsimile/electronic message is proprietary and confidential and is exclusively addressed to the named recipient(s). Any use, copying or distribution of the above referred information by any unintended recipient may be illicit and result in damage, harm and loss to the sender and/or to the intended recipient(s). If you have received this message in error please immediately notify us.

-----Original Message-----

The permission below is for the use of Table 1.1.

nperez21@outlook.com

Sent: Monday, June 21, 2021 5:18 AM
To: nperez21@outlook.com
Cc: Claire Wilshaw
Subject: ACI212061 - Renal Denervation System/Patel - Permission Granted

Dear Dr. Noel Perez

Thank you for your below enquiry.

I am pleased to confirm that we grant permission to use table 1 for your dissertation and at no cost.

Renal denervation for the management of resistant hypertension
Patel H et al
Inegrated Blood Pressure Control 2015 8 57-69

Please note:

- The table must be fully cited
- Dove Medical Press must be acknowledged as the original publisher
- Any other re-use in the future will require separate permission to be requested
- No transfer of copyright should be inferred or implied

Please let me know should you have any further questions and I wish you all the best with your dissertation and studies.

Best Regards

Shannon

Shannon Ainsworth
Reprints Team
Dove Medical Press Limited

Beechfield House,
Winterton Way,
Macclesfield SK11 0LP
United Kingdom
www.dovepress.com

Company registration number: 4967856
Registered in England and Wales. Registered address 5 Howick Place, London, SW1P 1WG.
VAT Number: GB 365 4626 36

Dove Medical Press is part of Taylor & Francis Group, the Academic Publishing Division of Informa PLC

T: +44 (0)1625 509134
F: +44 (0)1625 617933

E: shannonainsworth@dovepress.co.uk

The information in this facsimile/electronic message is proprietary and confidential and is exclusively addressed to the named recipient(s). Any use, copying or distribution of the above referred information by any unintended recipient may be illicit and result in damage, harm and loss to the sender and/or to the intended recipient(s). If you have received this message in error please immediately notify us.

The permission below is for the use of Figure 3.1.

**JOHN WILEY AND SONS LICENSE
TERMS AND CONDITIONS**

May 15, 2021

This Agreement between Noel Perez ("You") and John Wiley and Sons ("John Wiley and Sons") consists of your license details and the terms and conditions provided by John Wiley and Sons and Copyright Clearance Center.

License Number 5070310150432

License date May 15, 2021

Licensed Content John Wiley and Sons
Publisher

Licensed Content Medical Physics
Publication

Licensed Content Evaluation of a tissue-mimicking thermochromic phantom for
Title radiofrequency ablation

Licensed Content Ari Partanen, Bradford J. Wood, Manoj Mathew, et al
Author

Licensed Content Jun 17, 2016
Date

Licensed Content 43
Volume

Licensed Content 7
Issue

Licensed Content 8
Pages

About the Author

Noel Perez received his BS in Electrical Engineering from the University of Puerto Rico, Mayagüez Campus (UPRM) 1990, MS in Engineering Management, and MS Manufacturing Engineering from Polytechnic University of Puerto Rico. A PhD at the University of South Florida in 2021. Noel currently works as a Vice President of Research and Development at Oscor, Inc., a global medical devices designer and manufacturer located at Palm Harbor, Florida.